NUREG/CR-6643
ORNL/TM-1999/297

Heavy-Section Steel Irradiation Program

Hardening Behavior of Ferritic Alloys at High Doses and After Thermal Aging

Oak Ridge National Laboratory

U.S. Nuclear Regulatory Commission
Office of Nuclear Regulatory Research
Washington, DC 20555-0001

AVAILABILITY NOTICE

Availability of Reference Materials Cited in NRC Publications

NRC publications in the NUREG series, NRC regulations, and *Title 10, Energy,* of the *Code of Federal Regulations,* may be purchased from one of the following sources:

1. The Superintendent of Documents
   U.S. Government Printing Office
   P.O. Box 37082
   Washington, DC 20402–9328
   <http://www.access.gpo.gov/su_docs>
   202–512–1800
2. The National Technical Information Service
   Springfield, VA 22161–0002
   <http://www.ntis.gov>
   1–800–553–6847 or locally 703–605–6000

The NUREG series comprises (1) brochures (NUREG/BR-XXXX), (2) proceedings of conferences (NUREG/CP-XXXX), (3) reports resulting from international agreements (NUREG/IA-XXXX), (4) technical and administrative reports and books [(NUREG-XXXX) or (NUREG/CR-XXXX)], and (5) compilations of legal decisions and orders of the Commission and Atomic and Safety Licensing Boards and of Office Directors' decisions under Section 2.206 of NRC's regulations (NUREG-XXXX).

A single copy of each NRC draft report for comment is available free, to the extent of supply, upon written request as follows:

Address: Office of the Chief Information Officer
Reproduction and Distribution
Services Section
U.S. Nuclear Regulatory Commission
Washington, DC 20555–0001
E–mail: <DISTRIBUTION@nrc.gov>
Facsimile: 301–415–2289

A portion of NRC regulatory and technical information is available at NRC's World Wide Web site:

<http://www.nrc.gov>

After January 1, 2000, the public may electronically access NUREG-series publications and other NRC records in NRC's Agencywide Document Access and Management System (ADAMS), through the Public Electronic Reading Room (PERR), link <http://www.nrc.gov/NRC/ADAMS/index.html>.

Publicly released documents include, to name a few, NUREG-series reports; *Federal Register* notices; applicant, licensee, and vendor documents and correspondence; NRC correspondence and internal memoranda; bulletins and information notices; inspection and investigation reports; licensee event reports; and Commission papers and their attachments.

Documents available from public and special technical libraries include all open literature items, such as books, journal articles, and transactions, *Federal Register* notices, Federal and State legislation, and congressional reports. Such documents as theses, dissertations, foreign reports and translations, and non-NRC conference proceedings may be purchased from their sponsoring organization.

Copies of industry codes and standards used in a substantive manner in the NRC regulatory process are maintained at the NRC Library, Two White Flint North, 11545 Rockville Pike, Rockville, MD 20852–2738. These standards are available in the library for reference use by the public. Codes and standards are usually copyrighted and may be purchased from the originating organization or, if they are American National Standards, from—

American National Standards Institute
11 West 42nd Street
New York, NY 10036–8002
<http://www.ansi.org>
212–642–4900

DISCLAIMER

This report was prepared as an account of work sponsored by an agency of the United States Government. Neither the United States Government nor any agency thereof, nor any of their employees, makes any warranty, expressed or implied, or assumes any legal liability or responsibility for any third party's use, or the results of such use, of any information, apparatus, product, or process disclosed in this report, or represents that its use by such third party would not infringe privately owned rights.

NUREG/CR-6643
ORNL/TM-1999/297

Heavy-Section Steel Irradiation Program

Hardening Behavior of Ferritic Alloys at High Doses and After Thermal Aging

Manuscript Completed: April 2000

Date Published:

Prepared by
P. M. Rice and R. E. Stoller

Oak Ridge National Laboratory
Managed by UT-Battelle, LLC
Oak Ridge, TN 37831-6138

C. J. Fairbanks, NRC Project Manager

Prepared for
Division of Engineering Technology
Office of Nuclear Regulatory Research
U.S. Nuclear Regulatory Commission
Washington, DC 20555-0001
NRC Job Code W6953.

NUREG/CR-6643 has been reproduced from the best available copy.

Abstract

A series of high-dose iron and helium ion irradiation experiments were carried out to investigate the effects of minor solutes on the irradiation response of model ferritic alloys. The irradiated microstructure was characterized by transmission electron microscopy and radiation-induced hardening was measured using an ultra-low load indentation technique. The low load technique with its corresponding low indentation depth was required because the thickness of the irradiated layer was only 1 to 4 μm. An attempt was made to correlate the observed microstructural changes with the measured hardness changes, and reasonable values were obtained for strength of small interstitial loops as dislocation barriers in the copper-free materials. However, the addition of copper to iron was found to greatly refine the radiation-induced microstructure. Although further additions of either interstitial or substitutional solutes tended to coarsen it again, the presence of a defect structure that was too small to be resolved by TEM limited the microstructure-mechanical property correlation efforts. The helium ion irradiations revealed a very strong copper-vacancy binding interaction that is relevant to the formation of copper-enriched precipitates in irradiated steels.

CONTENTS

FIGURES

Page

TABLES

Page

ACKNOWLEDGMENTS

The authors would like to thank Drs. R. K. Nanstad and D. T. Hoelzer for helpful discussions and for reviewing this document, Dr. J. Bentley for his assistance with the GIF analysis, and Profs. G. R. Odette and G. E. Lucas from the University of California, Santa Barbara, for supplying the alloys used in this work.

The continuing support of the Office of Nuclear Regulatory Research, U. S. Nuclear Regulatory Commission, is gratefully acknowledged. Contributions to this work were supported in part by the Division of Materials Sciences, U. S. Department of Energy, under contract DE-AC05-96OR22464 with Lockheed Martin Energy Research Corp., published under contract DE-AC05-00OR22725 with UT-Battelle, LLC, and by an appointment of P. M. Rice to the Oak Ridge National Laboratory Postdoctoral Research Associates Program administered jointly by the Oak Ridge National Laboratory and the Oak Ridge Institute for Science and Education.

FOREWORD

The work reported here was performed at the Oak Ridge National Laboratory (ORNL) under the Heavy-Section Steel Irradiation (HSSI) Program, T. M. Rosseel, Program Manager. The program is sponsored by the Office of Nuclear Regulatory Research of the U.S. Nuclear Regulatory Commission (NRC). The technical monitor for the NRC is C. J. Fairbanks.

This report is designated HSSI Report 26. Reports in this series are listed below:

1. F. M. Haggag, W. R. Corwin, and R. K. Nanstad, Martin Marietta Energy Systems, Inc., Oak Ridge Natl. Lab., Oak Ridge, Tenn., *Irradiation Effects on Strength and Toughness of Three-Wire Series-Arc Stainless Steel Weld Overlay Cladding*, USNRC Report NUREG/CR-5511 (ORNL/TM-11439), February 1990.

2. L. F. Miller, C. A. Baldwin, F. W. Stallman, and F. B. K. Kam, Martin Marietta Energy Systems, Inc., Oak Ridge Natl. Lab., Oak Ridge, Tenn., *Neutron Exposure Parameters for the Metallurgical Test Specimens in the Sixth Heavy-Section Steel Irradiation Series*, USNRC Report NUREG/CR-5409 (ORNL/TM-11267), March 1990.

3. S. K. Iskander, W. R. Corwin, and R. K. Nanstad, Martin Marietta Energy Systems, Inc., Oak Ridge Natl. Lab., Oak Ridge, Tenn., *Results of Crack-Arrest Tests on Two Irradiated High-Copper Welds*, USNRC Report NUREG/CR-5584 (ORNL/TM-11575), December 1990.

4. R. K. Nanstad and R. G. Berggren, Martin Marietta Energy Systems, Inc., Oak Ridge Natl. Lab., Oak Ridge, Tenn., *Irradiation Effects on Charpy Impact and Tensile Properties of Low Upper-Shelf Welds, HSSI Series 2 and 3*, USNRC Report NUREG/CR-5696 (ORNL/TM-11804), August 1991.

5. R. E. Stoller, Martin Marietta Energy Systems, Inc., Oak Ridge Natl. Lab., Oak Ridge, Tenn., *Modeling the Influence of Irradiation Temperature and Displacement Rate on Radiation-Induced Hardening in Ferritic Steels,* USNRC Report NUREG/CR5859 (ORNL/TM-12073), August 1992.

6. R. K. Nanstad, D. E. McCabe, and R. L. Swain, Martin Marietta Energy Systems, Inc., Oak Ridge Natl. Lab., Oak Ridge, Tenn., *Chemical Composition RT_{NDT} Determinations for Midland Weld WF-70*, USNRC Report NUREG/CR-5914 (ORNL-6740), December 1992.

7. R. K. Nanstad, F. M. Haggag, D. E. McCabe, S. K. Iskander, K. O. Bowman, and B. H. Menke, Martin Marietta Energy Systems, Inc., Oak Ridge Natl. Lab., Oak Ridge, Tenn., *Irradiation Effects on Fracture Toughness of Two High-Copper Submerged-Arc Welds,* USNRC Report NUREG/CR-5913 (ORNL/TM-12156/V1), October 1992.

8. S. K. Iskander, W. R. Corwin, and R. K. Nanstad, Martin Marietta Energy Systems, Inc., Oak Ridge Natl. Lab., Oak Ridge, Tenn., *Crack-Arrest Tests on Two Irradiated High-Copper Welds*, USNRC Report NUREG/CR-6139 (ORNL/TM-12513), March 1994.

9. R. E. Stoller, Martin Marietta Energy Systems, Inc., Oak Ridge Natl. Lab., Oak Ridge, Tenn., *A Comparison of the Relative Importance of Copper Precipitates and Point Defects in Reactor Pressure Vessel Embrittlement,* USNRC Report NUREG/CR-6231 (ORNL/TM-6811), December 1994.

10. D. E. McCabe, R. K. Nanstad, S. K. Iskander, and R. L. Swain, Martin Marietta Energy Systems, Inc., Oak Ridge Natl. Lab., Oak Ridge, Tenn., *Unirradiated Material Properties of Midland Weld WF-70,* USNRC Report NUREG/CR-6249 (ORNL/TM-12777), October 1994.

11. P. M. Rice and R. E. Stoller, Lockheed Martin Energy Systems, Oak Ridge Natl. Lab., Oak Ridge, Tenn., *Microstructural Characterization of Selected AEA/UCSB Model FeCuMn Alloys,* USNRC Report NUREG/CR-6332 (ORNL/TM-12980), June 1996.

12. J. H. Giovanola and J. E. Crocker, SRI International, *Fracture Toughness Testing with Cracked Round Bars: Feasibility Study*, USNRC Report NUREG/CR-6342 (ORNL/SUB/94-DHK60), April 2000.

13. F. M. Haggag and R. K. Nanstad, Lockheed Martin Energy Systems, Oak Ridge Natl. Lab., Oak Ridge, Tenn., *Effects of Thermal Aging and Neutron Irradiation on the Mechanical Properties of Three-Wire Stainless Steel Weld Overlay Cladding,* USNRC Report NUREG/CR-6363 (ORNL/TM-13047), May 1997.

14. M. A. Sokolov and D. J. Alexander, Lockheed Martin Energy Systems, Oak Ridge Natl. Lab., Oak Ridge, Tenn., *An Improved Correlation Procedure for Subsize and Full-Size Charpy Impact Specimen Data,* USNRC Report NUREG/CR-6379 (ORNL/TM-13088), March 1997.

15. S. K. Iskander and R. E. Stoller, Lockheed Martin Energy Research Corporation, Oak Ridge Natl. Lab., Oak Ridge, Tenn., *Results of Charpy V-Notch Impact Testing of Structural Steel Specimens Irradiated at ~30°C to 1 $\times$ 10^{16} Neutrons/cm^2 in a Commercial Reactor Cavity*, USNRC Report NUREG/CR-6399 (ORNL-6886), April 1997.

16. S. K. Iskander, P. P. Milella, and A. Pini, Lockheed Martin Energy Research Corporation, Oak Ridge Natl. Lab., Oak Ridge, Tenn., *Results of Crack-Arrest Tests on Irradiated A 503 Class 3 Steel*, USNRC Report NUREG/CR-6447 (ORNL-6894), February 1998.

17. P. Pareige, K. F. Russell, R. E. Stoller, and M. K. Miller, Lockheed Martin Energy Research Corporation, Oak Ridge Natl. Lab., Oak Ridge, Tenn., *Influence of Long-Term Thermal Aging on the Microstructural Evolution of Nuclear Reactor Pressure Vessel Materials: An Atom Probe Study*, USNRC Report NUREG/CR-6537 (ORNL-13406), March 1998.

18. I. Remec, C. A. Baldwin, and K. B. K. Kam, Lockheed Martin Energy Research Corporation, Oak Ridge Natl. Lab., Oak Ridge, Tenn., *Neutron Exposure Parameters for Capsule 10.05 in the Heavy-Section Steel Irradiation Program Tenth Irradiation Series*, USNRC Report NUREG/CR-6600 (ORNL/TM-13548), October 1998.

19. I. Remes, C. A. Baldwin, and F. B. K. Kam, Lockheed Martin Energy Research Corporation, Oak Ridge Natl. Lab., Oak Ridge, Tenn., *Neutron Exposure Parameters for the Dosimetry Capsule in the Heavy-Section Steel Irradiation Program Tenth Irradiation Series*, USNRC Report NUREG/CR-6601 (ORNL/TM-13549), October 1998.

20. D. E. McCabe, R. K. Nanstad, S. K. Iskander, D. W. Heatherly, and R. L. Swain, Lockheed Martin Energy Research Corporation, Oak Ridge Natl. Lab., Oak Ridge, Tenn., *Evaluation of WF-70 Weld Metal from the Midland Unit 1 Reactor Vessel-Final Report*, USNRC Report NUREG/CR-5736 (ORNL/TM-13748), to be published.

21. Mikhail A. Sokolov and Randy K. Nanstad, Lockheed Martin Energy Research Corporation, Oak Ridge Natl. Lab., Oak Ridge, Tenn., *Comparison of Irradiation-Induced Shifts of K_{Jc} and Charpy Impact Toughness for Reactor Pressure Vessel Steels*, USNRC Report NUREG/CR-6609 (ORNL/TM-13755), to be published.

22. S. K. Iskander, C. A. Baldwin, D. W. Heatherly, D. E. McCabe, I. Remec, and R. L. Swain, Lockheed Martin Energy Research Corporation, Oak Ridge Natl. Lab., Oak Ridge, Tenn., *Detailed Results of Testing Unirradiated and Irradiated Crack-Arrest Toughness Specimens from the Low Upper-Shelf Energy, High Copper Weld, WF-70*, USNRC Report NUREG/CR-6621 (ORNL/TM-13764), to be published.

23. D. J. Alexander, K. B. Alexander, M. K. Miller, and R. K. Nanstad, Lockheed Martin Energy Research Corporation, Oak Ridge Natl. Lab., Oak Ridge, Tenn., *The Effect of Aging at 343°C on the Microstructure and Mechanical Properties of Type 308 Stainless Steel Welds,* USNRC Report NUREG/CR-6628 (ORNL/TM-13767), to be published.

24. M. K. Miller, P. Pariege, K. F. Russell, and R. E. Stoller, Lockheed Martin Energy Research Corporation, Oak Ridge Natl. Lab., Oak Ridge, Tenn., *An Atom Probe Tomography Characterization of the Solute Distributions in a Neutron Irradiated and Annealed Pressure Vessel Steel,* USNRC Report NUREG/CR-6629 (ORNL/TM-13768), to be published.

25. I. Remic, C. A. Baldwin, and E. D. Blakeman, Lockheed Martin Energy Research Corporation, Oak Ridge Natl. Lab., Oak Ridge, Tenn., *Characterizaion of the Neutron Field in the HSSI/UCSB Irradiation Facility at the ford Nuclear Reactor,* USNRC Report NUREG/CR-6646 (ORNL/TM 1999/140), to be published.

26. This report.

The HSSI Program includes both follow-on and the direct continuation of work that was performed under the Heavy-Section Steel Technology (HSST) Program. Previous HSST reports related to irradiation effects in pressure vessel materials and those containing unirradiated properties of materials used in HSSI and HSST irradiation programs are tabulated below as a convenience to the reader.

C. E. Childress, Union Carbide Corp. Nuclear Div., Oak Ridge Natl. Lab., Oak Ridge, Tenn., *Fabrication History of the First Two 12-in.-Thick A-533 Grade B, Class 1 Steel Plates of the Heavy-Section Steel Technology Program*, ORNL-4313, February 1969.

T. R. Mager and F. O. Thomas, Westinghouse Electric Corporation, PWR Systems Division, Pittsburgh, Pa., *Evaluation by Linear Elastic Fracture Mechanics of Radiation Damage to Pressure Vessel Steels*, WCAP-7328 (Rev.), October 1969.

P. N. Randall, TRW Systems Group, Redondo Beach, Calif., *Gross Strain Measure of Fracture Toughness of Steels*, HSSTP-TR-3, Nov. 1, 1969.

L. W. Loechel, Martin Marietta Corporation, Denver, Colo., *The Effect of Testing Variables on the Transition Temperature in Steel*, MCR-69-189, Nov. 20, 1969.

W. O. Shabbits, W. H. Pryle, and E. T. Wessel, Westinghouse Electric Corporation, PWR Systems Division, Pittsburgh, Pa., *Heavy-Section Fracture Toughness Properties of A533 Grade B Class 1 Steel Plate and Submerged Arc Weldment*, WCAP-7414, December 1969.

C. E. Childress, Union Carbide Corp. Nuclear Div., Oak Ridge Natl. Lab., Oak Ridge, Tenn., *Fabrication History of the Third and Fourth ASTM A-533 Steel Plates of the Heavy-Section Steel Technology Program*, ORNL-4313-2, February 1970.

P. B. Crosley and E. J. Ripling, Materials Research Laboratory, Inc., Glenwood, Ill., *Crack Arrest Fracture Toughness of A533 Grade B Class 1 Pressure Vessel Steel*, HSSTP-TR-8, March 1970.

F. J. Loss, Naval Research Laboratory, Washington, D.C., *Dynamic Tear Test Investigations of the Fracture Toughness of Thick-Section Steel*, NRL-7056, May 14, 1970.

T. R. Mager, Westinghouse Electric Corporation, PWR Systems Division, Pittsburgh, Pa., *Post-Irradiation Testing of 2T Compact Tension Specimens*, WCAP-7561, August 1970.

F. J. Witt and R. G. Berggren, Union Carbide Corp. Nuclear Div., Oak Ridge Natl. Lab., Oak Ridge, Tenn., *Size Effects and Energy Disposition in Impact Specimen Testing of ASTM A533 Grade B Steel*, ORNL/TM-3030, August 1970.

D. A. Canonico, Union Carbide Corp. Nuclear Div., Oak Ridge Natl. Lab., Oak Ridge, Tenn., *Transition Temperature Considerations for Thick-Wall Nuclear Pressure Vessels,* ORNL/TM-3114, October 1970.

T. R. Mager, Westinghouse Electric Corporation, PWR Systems Division, Pittsburgh, Pa., *Fracture Toughness Characterization Study of A533, Grade B, Class 1 Steel*, WCAP-7578, October 1970.

W. O. Shabbits, Westinghouse Electric Corporation, PWR Systems Division, Pittsburgh, Pa., *Dynamic Fracture Toughness Properties of Heavy-Section A533 Grade B Class 1 Steel Plate*, WCAP-7623, December 1970.

C. E. Childress, Union Carbide Corp. Nuclear Div., Oak Ridge Natl. Lab., Oak Ridge, Tenn., *Fabrication Procedures and Acceptance Data for ASTM A-533 Welds and a 10-in.-Thick ASTM A-543 Plate of the Heavy Section Steel Technology Program*, ORNL-TM-4313-3, January 1971.

D. A. Canonico and R. G. Berggren, Union Carbide Corp. Nuclear Div., Oak Ridge Natl. Lab., Oak Ridge, Tenn., *Tensile and Impact Properties of Thick-Section Plate and Weldments,* ORNL/TM-3211, January 1971.

C. W. Hunter and J. A. Williams, Hanford Eng. Dev. Lab., Richland, Wash., *Fracture and Tensile Behavior of Neutron-Irradiated A533-B Pressure Vessel Steel*, HEDL-TME-71-76, Feb. 6, 1971.

C. E. Childress, Union Carbide Corp. Nuclear Div., Oak Ridge Natl. Lab., Oak Ridge, Tenn., *Manual for ASTM A533 Grade B Class 1 Steel (HSST Plate 03) Provided to the International Atomic Energy Agency*, ORNL/TM-3193, March 1971.

P. N. Randall, TRW Systems Group, Redondo Beach, Calif., *Gross Strain Crack Tolerance of A533-B Steel*, HSSTP-TR-14, May 1, 1971.

C. L. Segaser, Union Carbide Corp. Nuclear Div., Oak Ridge Natl. Lab., Oak Ridge, Tenn., *Feasibility Study, Irradiation of Heavy-Section Steel Specimens in the South Test Facility of the Oak Ridge Research Reactor*, ORNL/TM-3234, May 1971.

H. T. Corten and R. H. Sailors, University of Illinois, Urbana, Ill., *Relationship Between Material Fracture Toughness Using Fracture Mechanics and Transition Temperature Tests*, T&AM Report 346, Aug. 1, 1971.

L. A. James and J. A. Williams, Hanford Eng. Dev. Lab., Richland, Wash., *Heavy Section Steel Technology Program Technical Report No. 21, The Effect of Temperature and Neutron Irradiation Upon the Fatigue-Crack Propagation Behavior of ASTM A533 Grade B, Class 1 Steel*, HEDL-TME 72-132, September 1972.

P. B. Crosley and E. J. Ripling, Materials Research Laboratory, Inc., Glenwood, Ill., *Crack Arrest in an Increasing K-Field*, HSSTP-TR-27, January 1973.

W. J. Stelzman and R. G. Berggren, Union Carbide Corp. Nuclear Div., Oak Ridge Natl. Lab., Oak Ridge, Tenn., *Radiation Strengthening and Embrittlement in Heavy-Section Steel Plates and Welds*, ORNL-4871, June 1973.

J. M. Steichen and J. A. Williams, Hanford Eng. Dev. Lab., Richland, Wash., *High Strain Rate Tensile Properties of Irradiated ASTM A533 Grade B Class 1 Pressure Vessel Steel*, HEDL-TME 73-74, July 1973.

J. A. Williams, Hanford Eng. Dev. Lab., Richland, Wash., *The Irradiation and Temperature Dependence of Tensile and Fracture Properties of ASTM A533, Grade B, Class 1 Steel Plate and Weldment*, HEDL-TME 73-75, August 1973.

J. A. Williams, Hanford Eng. Dev. Lab., Richland, Wash., *Some Comments Related to the Effect of Rate on the Fracture Toughness of Irradiated ASTM A553-B Steel Based on Yield Strength Behavior*, HEDL-SA 797, December 1974.

J. A. Williams, Hanford Eng. Dev. Lab., Richland, Wash., *The Irradiated Fracture Toughness of ASTM A533, Grade B, Class 1 Steel Measured with a Four-Inch-Thick Compact Tension Specimen*, HEDL-TME 75-10, January 1975.

J. G. Merkle, G. D. Whitman, and R. H. Bryan, Union Carbide Corp. Nuclear Div., Oak Ridge Natl. Lab., Oak Ridge, Tenn., *An Evaluation of the HSST Program Intermediate Pressure Vessel Tests in Terms of Light-Water-Reactor Pressure Vessel Safety*, ORNL/TM-5090, November 1975.

J. A. Davidson, L. J. Ceschini, R. P. Shogan, and G. V. Rao, Westinghouse Electric Corporation, Pittsburgh, Pa., *The Irradiated Dynamic Fracture Toughness of ASTM A533, Grade B, Class 1 Steel Plate and Submerged Arc Weldment*, WCAP-8775, October 1976.

J. A. Williams, Hanford Eng. Dev. Lab., Richland, Wash., *Tensile Properties of Irradiated and Unirradiated Welds of A533 Steel Plate and A508 Forgings*, NUREG/CR-1158 (ORNL/SUB-79/50917/2), July 1979.

J. A. Williams, Hanford Eng. Dev. Lab., Richland, Wash., *The Ductile Fracture Toughness of Heavy-Section Steel Plate*, NUREG/CR-0859, September 1979.

K. W. Carlson and J. A. Williams, Hanford Eng. Dev. Lab., Richland, Wash., *The Effect of Crack Length and Side Grooves on the Ductile Fracture Toughness Properties of ASTM A533 Steel*, NUREG/CR-1171 (ORNL/SUB-79/50917/3), October 1979.

G. A. Clarke, Westinghouse Electric Corp., Pittsburgh, Pa., *An Evaluation of the Unloading Compliance Procedure for J-Integral Testing in the Hot Cell, Final Report*, NUREG/CR-1070 (ORNL/SUB-7394/1), October 1979.

P. B. Crosley and E. J. Ripling, Materials Research Laboratory, Inc., Glenwood, Ill., *Development of a Standard Test for Measuring K_{Ia} with a Modified Compact Specimen*, NUREG/CR-2294 (ORNL/SUB-81/7755/1), August 1981.

H. A. Domian, Babcock and Wilcox Company, Alliance, Ohio, *Vessel V-8 Repair and Preparation of Low Upper-Shelf Weldment*, NUREG/CR-2676 (ORNL/SUB/81-85813/1), June 1982.

R. D. Cheverton, S. K. Iskander, and D. G. Ball, Union Carbide Corp. Nuclear Div., Oak Ridge Natl. Lab., Oak Ridge, Tenn., *PWR Pressure Vessel Integrity During Overcooling Accidents: A Parametric Analysis*, NUREG/CR-2895 (ORNL/TM-7931), February 1983.

J. G. Merkle, Union Carbide Corp. Nuclear Div., Oak Ridge Natl. Lab., Oak Ridge, Tenn., *An Examination of the Size Effects and Data Scatter Observed in Small Specimen Cleavage Fracture Toughness Testing*, NUREG/CR-3672 (ORNL/TM-9088), April 1984.

W. R. Corwin, Martin Marietta Energy Systems, Inc., Oak Ridge Natl. Lab., Oak Ridge, Tenn., *Assessment of Radiation Effects Relating to Reactor Pressure Vessel Cladding*, NUREG/CR-3671 (ORNL-6047), July 1984.

W. R. Corwin, R. G. Berggren, and R. K. Nanstad, Martin Marietta Energy Systems, Inc., Oak Ridge Natl. Lab., Oak Ridge, Tenn., *Charpy Toughness and Tensile Properties of a Neutron Irradiated Stainless Steel Submerged-Arc Weld Cladding Overlay*, NUREG/CR-3927 (ORNL/TM-9709), September 1984.

J. J. McGowan, Martin Marietta Energy Systems, Inc., Oak Ridge Natl. Lab., Oak Ridge, Tenn., *Tensile Properties of Irradiated Nuclear Grade Pressure Vessel Plate and Welds for the Fourth HSST Irradiation Series*, NUREG/CR-3978 (ORNL/TM-9516), January 1985.

J. J. McGowan, Martin Marietta Energy Systems, Inc., Oak Ridge Natl. Lab., Oak Ridge, Tenn., *Tensile Properties of Irradiated Nuclear Grade Pressure Vessel Welds for the Third HSST Irradiation Series*, NUREG/CR-4086 (ORNL/TM-9477), March 1985.

W. R. Corwin, G. C. Robinson, R. K. Nanstad, J. G. Merkle, R. G. Berggren, G. M. Goodwin, R. L. Swain, and T. D. Owings, Martin Marietta Energy Systems, Inc., Oak Ridge Natl. Lab., Oak Ridge, Tenn., *Effects of Stainless Steel Weld Overlay Cladding on the Structural Integrity of Flawed Steel Plates in Bending, Series 1*, NUREG/CR-4015 (ORNL/TM-9390), April 1985.

W. J. Stelzman, R. G. Berggren, and T. N. Jones, Martin Marietta Energy Systems, Inc., Oak Ridge Natl. Lab., Oak Ridge, Tenn., *ORNL Characterization of Heavy-Section Steel Technology Program Plates 01, 02, and 03*, NUREG/CR-4092 (ORNL/TM-9491), April 1985.

G. D. Whitman, Martin Marietta Energy Systems, Inc., Oak Ridge Natl. Lab., Oak Ridge, Tenn., *Historical Summary of the Heavy-Section Steel Technology Program and Some Related Activities in Light-Water Reactor Pressure Vessel Safety Research*, NUREG/CR-4489 (ORNL-6259), March 1986.

R. H. Bryan, B. R. Bass, S. E. Bolt, J. W. Bryson, J. G. Merkle, R. K. Nanstad, and G. C. Robinson, Martin Marietta Energy Systems, Inc., Oak Ridge Natl. Lab., Oak Ridge, Tenn., *Test of 6-in.-Thick Pressure Vessels. Series 3: Intermediate Test Vessel V-8A—Tearing Behavior of Low Upper-Shelf Material*, NUREG-CR-4760 (ORNL-6187), May 1987.

D. B. Barker, R. Chona, W. L. Fourney, and G. R. Irwin, University of Maryland, College Park, Md., *A Report on the Round Robin Program Conducted to Evaluate the Proposed ASTM Standard Test Method for Determining the Plane Strain Crack Arrest Fracture Toughness, K_{Ia}, of Ferritic Materials*, NUREG/CR-4966 (ORNL/SUB/79-7778/4), January 1988.

L. F. Miller, C. A. Baldwin, F. W. Stallman, and F. B. K. Kam, Martin Marietta Energy Systems, Inc., Oak Ridge Natl. Lab., Oak Ridge, Tenn., *Neutron Exposure Parameters for the Metallurgical Test Specimens in the Fifth Heavy-Section Steel Technology Irradiation Series Capsules*, NUREG/CR-5019 (ORNL/TM-10582), March 1988.

J. J. McGowan, R. K. Nanstad, and K. R. Thoms, Martin Marietta Energy Systems, Inc., Oak Ridge Natl. Lab., Oak Ridge, Tenn., *Characterization of Irradiated Current-Practice Welds and A533 Grade B Class 1 Plate for Nuclear Pressure Vessel Service*, NUREG/CR-4880 (ORNL-6484/V1 and V2), July 1988.

R. D. Cheverton, W. E. Pennell, G. C. Robinson, and R. K. Nanstad, Martin Marietta Energy Systems, Inc., Oak Ridge Natl. Lab., Oak Ridge, Tenn., *Impact of Radiation Embrittlement on Integrity of Pressure Vessel Supports for Two PWR Plants,* NUREG/CR-5320 (ORNL/TM-10966), February 1989.

J. G. Merkle, Martin Marietta Energy Systems, Inc., Oak Ridge Natl. Lab., Oak Ridge, Tenn., *An Overview of the Low-Upper-Shelf Toughness Safety Margin Issue*, NUREG/CR-5552 (ORNL/TM-11314), August 1990.

R. D. Cheverton, T. L. Dickson, J. G. Merkle, and R. K. Nanstad, Martin Marietta Energy Systems, Inc., Oak Ridge Natl. Lab., Oak Ridge, Tenn., *Review of Reactor Pressure Vessel Evaluation Report for Yankee Rowe Nuclear Power Station (YAEC No. 1735)*, NUREG/CR-5799 (ORNL/TM-11982), March 1992.

Hardening Behavior of Ferritic Alloys at High Doses and After Thermal Aging

Philip M. Rice and Roger E. Stoller

1 INTRODUCTION

This report describes a the results of a series of experiments carried out to investigate the role of chemical composition on radiation-induced hardening using a set of model ferritic alloys. The experiments involved both thermal aging and ion irradiations. The ion-irradiation experiments were undertaken to investigate the feasibility of using charged-particle irradiations as a tool for understanding irradiation effects in reactor pressure vessel (RPV) steels and for correlating observed microstructural changes with measured mechanical property changes. The potential advantages of such an approach arise primarily from the greatly accelerated damage rate that ion irradiations provide; these include the ability to (1) investigate high fluence (dose) effects, (2) rapidly evaluate a broad range of materials, and (3) perform microstructural examination of irradiated materials without having to deal with induced radioactivity.

The use of ion-irradiated specimens is well suited to microstructural investigation by transmission electron microscopy (TEM). However, special techniques are required to obtain mechanical property data from such specimens because the thickness of the irradiated area is on the order of a few micrometers. In this study, a very low-load hardness-measuring device called the NanoIndenter-II® was used.[1] This high-precision instrument measures the force required to drive a Berkovich diamond indenter as a function of penetration depth (displacement). In the case of ion-irradiated specimens, the change in hardness caused by the radiation damage was measured as a function of distance from the irradiated surface. The radiation-induced microstructure was characterized by TEM, and the microstructural observations were used to calculate the associated increment in hardening with a dispersed-barrier hardening model. The measured hardness change could then be compared to the calculated value.

The high dose rate obtained in ion irradiations provides the advantages mentioned above, but it also militates against a direct comparison with data obtained from commercial reactor surveillance programs. Dose-rate effects are generally well

understood in radiation-damage modeling. For example, it is well known that accelerated displacement rates can lead to an effective temperature shift in some radiation-induced phenomena.[2] An initial comparison of results obtained at 300 and 400^{o}C indicated that the difference in hardening was not significant for these two temperatures. Therefore, a decision was made to conduct the subsequent irradiations at 300^{o}C to help retain the fine-scale microstructure characteristic of the 280–300^{o}C RPV service temperature. However, it is not currently possible to predict precisely how to extrapolate from the ~10^{-6} dpa/s damage rates obtained in the ion-irradiation experiments to the ~10^{-10} dpa/s conditions experienced by commercial RPV materials. Thus, this work was undertaken to investigate radiation-damage mechanisms and the role of chemical composition rather than to simulate the neutron-irradiation conditions per se.

2 MATERIALS SELECTION

A set of 22 model ferritic alloys was prepared by AEA Technologies (AEAT) in the United Kingdom and the University of California, Santa Barbara (UCSB). These alloys encompassed systematic variations in copper, manganese, titanium, carbon, and nitrogen content. A high-purity iron from Blyth Metals Ltd. served as the base material. All alloying, including the nitrogen, was made by addition. Each ingot was heat-treated at 1100°C after casting and then hot forged to yield a billet of approximately 20 × 80 × 400 mm.

A subset of nine of these alloys was selected for use in the series of ion-irradiation experiments. The alloys were supplied to Oak Ridge National Laboratory (ORNL) by UCSB. The compositions of the nine alloys selected by ORNL are given in Table 1, along with their alloy designations and the base heat treatment carried out at UCSB. The solution treatment at 775°C was intended to put all the copper in solution in the α-phase

Table 1. Alloy designations and compositions

Alloy number	N (appm)	Composition (wt-%)			
		Cu	Mn	C	Ti
VM348	5	–	–	–	–
VM349	80	–	–	–	–
VM350	120	–	–	–	–
VM390	20	0.51	0.06	<0.005	0.002
VM397	20	0.91	<0.01	<0.01	<0.01
VM399	120	0.51	0.01	<0.01	<0.01
VM387	10	0.51	0.05	0.17	0.003
VM360	10	0.89	1.03	<0.003	–
VM373	100	<0.01	0.01	<0.003	0.3

As-Received Heat Treatment:

Solution treated at 775^{o}C for 17 h.

Quenched in salt bath to 450^{o}C and held for 3 min.

Air-cooled.

field, and the rapid quench was carried out to maintain a high level of dissolved copper. A short temper at 450°C was intended to precipitate carbon in the form of dispersed Fe_3C or M_3C intergranular carbides in the carbon-containing alloys.

These alloys have been extensively used by UCSB in neutron-irradiation experiments[3] and by AEAT in thermal-aging studies.[4] The UCSB heat treatment was somewhat different from the base heat treatment applied to these same alloys by AEAT. The AEAT solution treatment was similar, 16 h at 770°C, but their material was water quenched.[4,5] A comparison of our aging studies of alloy VM397 with that conducted by AEAT suggests that the AEAT solution treatment maintained a greater fraction of the copper in solution while the UCSB's 450°C temper and slower air-cooling may have initiated some copper precipitation.

The as-received microstructure of the alloy was characterized by TEM. An extensive description of the observations was published in NUREG/CR-6332.[6] A brief summary of the as-received materials is included here for completeness.

The major microstructural observations for the nine alloys were generally consistent with expectations of clean model alloys. Although TEM measurements of grain size are less accurate than those obtained by conventional metallography, our observations were similar to those reported by AEAT.[4] The grain sizes were generally large, ~ 100 μm. Exceptions were VM348, which exhibited a duplex structure; VM390, which exhibited a finer grain size due to many low-angle boundaries; and VM360 and VM373, which both showed slightly smaller grain size of ~50 μm. Detailed dislocation measurements were not made on all alloys, but the dislocation densities that were measured in VM348, VM349, and VM350 were quite low, ~10^{13} m^{-2}. Figure 1 shows the general microstructure of the low-nitrogen alloys with different copper levels.

The total precipitate density was low in most of the alloys, typically 1 to 7 $\times$ 10^{18} m^{-3}. The precipitates were primarily oxide or sulfide inclusions incorporating trace metallic impurities.

The authors have chosen to call the other main precipitate type observed in these alloys “carbo-nitride flakes,” meaning they are either ε-carbide platelets, α-nitride platelets, or a combination of both. Higher densities of carbo-nitrides were observed in the alloys

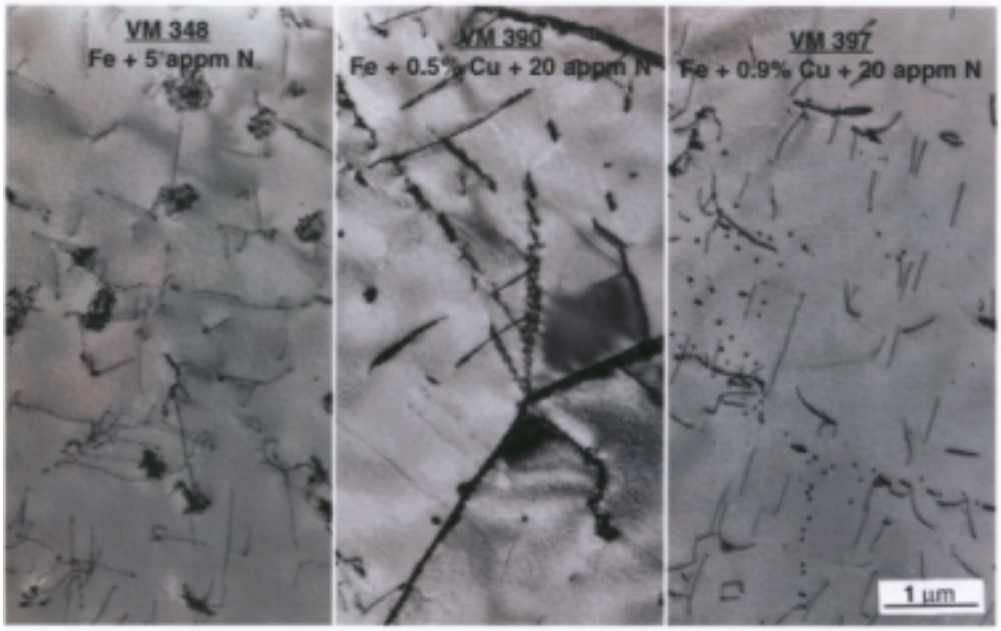

Figure 1. Typical "as-received" microstructures observed for the low-nitrogen alloys as marked. The copper concentration increases from left to right. All images are at the same magnification.

containing large amounts of nitrogen, as shown by the first two images in Figure 2. The first two images in Figure 2 show the typical microstructure of the high-nitrogen alloys with 0 and 0.5 wt-% copper. The third image shows the microstructure of the high-carbon alloy VM387, which shows only a slight amount of carbo-nitride formation. The significant difference between the size and density of the platelets in the high-nitrogen alloys as compared with those in the high-carbon alloy strongly suggests that the platelets are predominantly α-nitride rather than ε-carbide. Analytical electron microscopy results also strongly suggest that α-nitride precipitation was preferred over ε-carbide precipitation.[7]

Although many of the solutes were present only at the level of impurities, some conclusions about the effects of these various alloying elements on the observed microstructure were drawn in the previously published study.[6] One of the major effects of increasing the N content was to increase significantly the intergranular oxide formation and its associated carbo-nitride formation. Increasing the N content in the Cu-containing alloys increased the ratio of Cr to Mn in the oxide particles. However, increasing the Cu content in the low-N alloys seemed to decrease the ratio of Cr to Mn in the oxide formation.

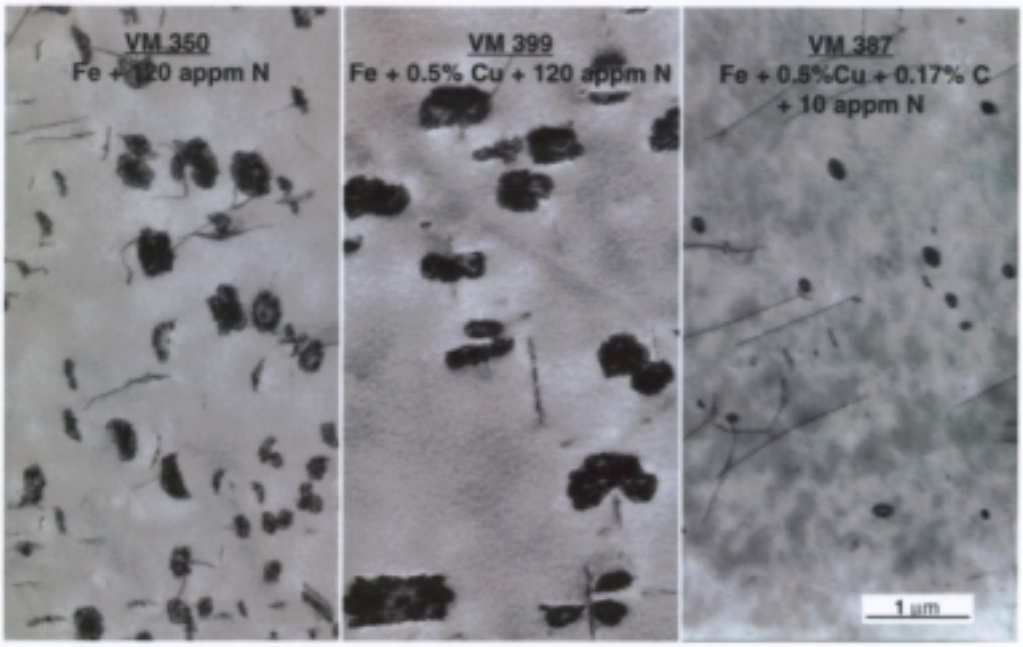

Figure 2. Typical "as-received" microstructure observed for the high-nitrogen or carbon-containing alloys as marked. Carbo-nitride precipitates are clearly visible in each alloy. All images are at the same magnification.

Other comparisons among the alloys are possible, but there were few systematic variations. The most obvious effect due to the increased carbon content was the increase in cementite (Fe_3C) formation, which was only rarely seen in the other alloys. The intergranular oxide formation was replaced by TiC precipitation, and surprisingly the carbo-nitride formation seemed to be slightly reduced. The addition of Ti was observed to eliminate the carbo-nitride formation.

3 EXPERIMENTAL TECHNIQUES

This section describes the techniques used to acquire the results that are presented in this report. The initial irradiation experiments were conducted with Fe-ion irradiations. Based on the experience obtained with these irradiated specimens, a decision was made to perform further irradiations using a light-ion beam to obtain a larger irradiation volume. These subsequent irradiations were conducted using a He ion beam. A brief section is included to describe the lessons learned from the Fe ion-irradiation experiments.

3.1 Specimen Preparation

Specimens were prepared for ion irradiation as follows. First, 3-mm-diam discs were punched from 0.5-mm-thick coupons of the as-received material. These were then mechanically ground to 0.38-mm thickness and mechanically polished with successively finer polishing solutions (down to 0.05-μm alumina [Linde B]) before receiving a final electrochemical polish using a perchloric-acid-based solution.

Because the irradiated area is relatively thin, specimens were prepared to expose the irradiated volume in cross section. This technique requires electroplating of the disc specimens to increase the thickness parallel to the beam direction, followed by sectioning to produce discs that then have the irradiated area exposed. A two-part plating procedure was followed. First, the specimens were electroplated with a thin layer of iron, and then with about 1 to 2 mm of nickel. The iron plating is necessary to ensure a smooth interface between the specimen and the subsequent thicker nickel plating. This is required to obtain a smoothly polished surface for nano-indentation, and an even polishing rate for TEM specimen preparation. Using nickel plating to provide the bulk of the additional material reduces the amount of magnetic material introduced into the microscope during TEM analysis.

The plated specimens were then sliced into specimens approximately 0.25 mm thick using a diamond wafering saw. One of the slices was polished in the same manner as described above, so that the surface around the interface was smooth enough to conduct the hardness measurements. An electro-discharge machine was used to cut 3-mm-diam TEM discs out of the other slices. The TEM discs were ground and sanded to 0.1 mm (0.004 in) thickness to minimize the amount of ferromagnetic material later

placed in the TEM. The specimens were then electrochemically thinned to electron transparency using a chilled perchloric electrolyte in a twin jet polisher. The composition of the electrolyte was 600 ml methanol, 340 ml butyl cellusolve, 60 ml perchloric acid, and 5 ml glycerine. The electrolyte was maintained at a temperature of –55^{o}C throughout the polishing and was stored in a freezer between uses to limit chemical reactions with the material removed from the specimens. A schematic diagram of the specimen preparation process is shown in Figure 3.

3.2 Measuring Hardness Changes

Specimens were prepared to expose the irradiated area in cross section as described above, and the change in hardness caused by the radiation damage was measured using the NanoIndenter-II® as a function of distance from the irradiated surface. This is a fully automated, ultra-low-load microindentation tester that precisely measures the force required to drive a Berkovich (triangular-base pyramid) diamond indenter to a prescribed depth.[1] The load and displacement can be measured with resolutions of 30 μg and

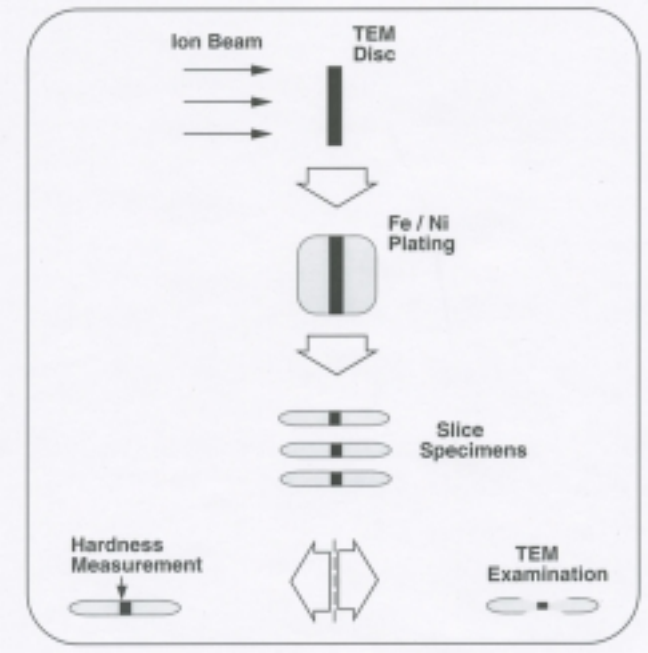

Figure 3. Schematic of specimen preparation steps for TEM examination and hardness measurements following ion irradiation.

0.16 nm, respectively. For the alloys tested here, loads ranging from 0.022 g to 0.043 g were required to reach an indent depth of 50 nm. Corresponding higher loads were required for deeper indents.

For the Fe irradiations the following method was used. Starting several microns away from the damaged region, measurements were taken approximately 5 μm apart along a line with a very shallow angle to the interface such that each indent was approximately 0.1 μm closer to the interface (i.e., the originally irradiated surface) until the interface was crossed. The measurements were made with indents having nominal depths of 30 nm, 50 nm, 75 nm, and 100 nm taken at the same position. The distance of the indents from the interface was measured using micrographs taken with a scanning electron microscope (SEM), like the one shown in Figure 4.

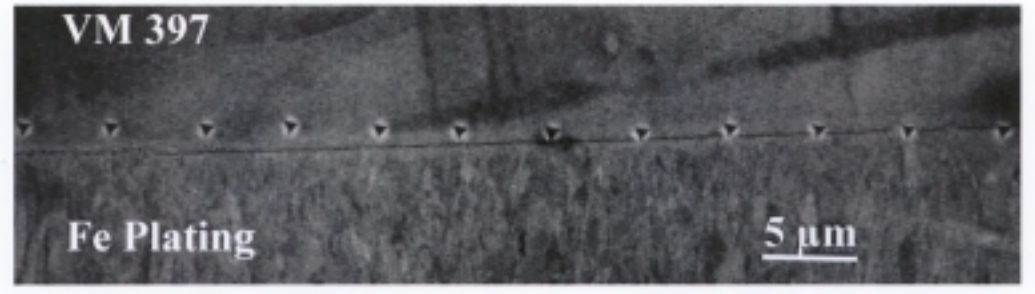

Figure 4. SEM image showing indents across the irradiated region of an iron-ion-irradiated specimen.

Only the indents with the 50-nm contact depth proved to provide both sufficient spatial resolution and the ability to produce hardness data with acceptable scatter to be of use in this investigation. The 30-nm hardness data tend to have too great a scatter due to interference from a thin oxide layer. The 75-nm and 100-nm indents sample too great a volume and thus do not have the desired spatial resolution.

An example of a hardness trace from VM390, the low-N alloy with 0.5 wt-% Cu, which was irradiated with iron ions to a peak dose of 0.2 dpa, is shown in Figure 5. The solid dots represent the measured values, which have been smoothed for the purpose of displaying the data by averaging each value with four adjacent data points, two on either side. Typically, the hardness of the unirradiated material was obtained as the average of several indents placed beyond the end of range of the ion beam. This is more than 2 and

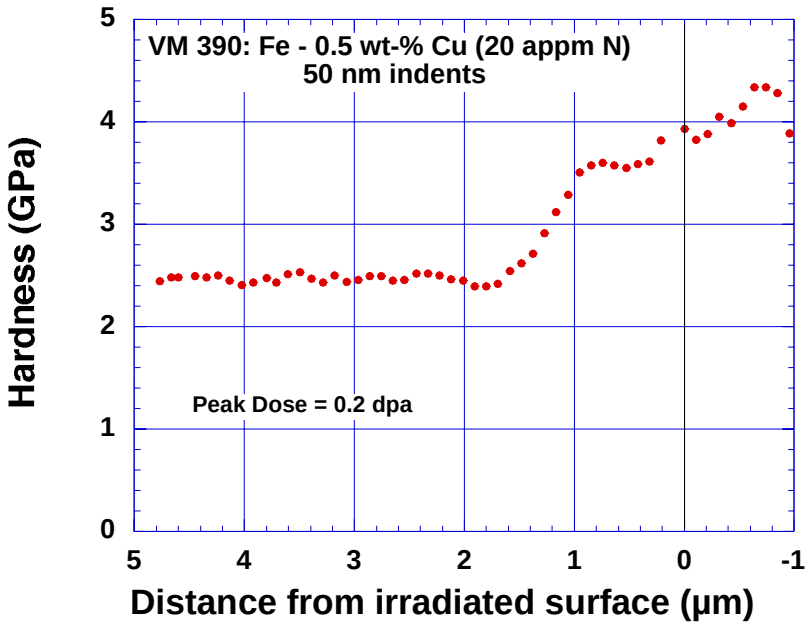

Figure 5. Hardness as a function of distance from the irradiated surface for a typical specimen of alloy VM390 irradiated with 4-MeV Fe ions to a peak dose of 0.2 dpa.

5 μm from the interface for Fe and He ion irradiations, respectively. This value is subtracted from the average of the three or four points at the peak of hardness to determine the change in hardness, ΔH.

In the case of the helium-ion irradiations, a similar row of approximately 100 indents was made at a very shallow angle to the original irradiated surface, starting a few microns beyond the irradiated region and ending in the electroplated layer of Fe at the specimen surface, as shown in Figure 6. Figure 6(*a*) is an SEM image of a typical row of indents in one of the model alloys showing the large-grained alloy on top and the fine-grained electroplate on the bottom. The dark band that the indents cross marks the end of range of the He ions and is visible due to grooving (i.e., preferential polishing during the electrochemical polishing process) caused by the high concentration of He bubbles in the region. The broken white line is the oxide that grew on the original irradiated surface. Figure 6(*b*) is a higher-magnification SEM image of the same set of indents where they

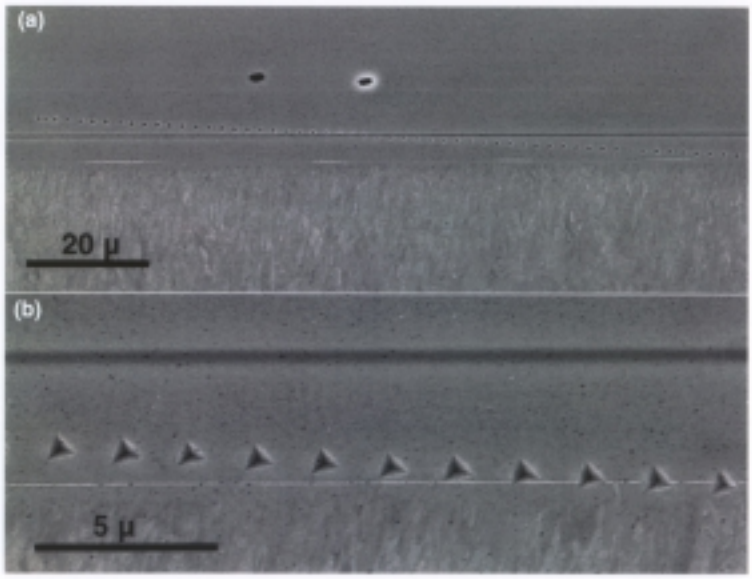

Figure 6. SEM images of a typical indentation run on one of the model alloys following helium ion irradiation: (*a*) low magnification view showing the entire indent run from beyond the irradiated region on the left into the electroplating on the right, and (*b*) higher magnification image of the indents at the end of the run. (The indents are ~100 nm deep, twice that used to acquire the change in hardness data.)

cross the original irradiated surface and enter the electroplate. Images like this one were used to measure each indent's position with respect to the original irradiated surface, which will be referred to as the "depth" in the remainder of the report.

Figure 7 shows a set of hardness measurements from the Cu-free, low-N alloy VM348, taken with indents having contact depths of ~50 nm. The indents were done at this contact depth to ensure that a constant and reasonable volume of material was sampled. The hardness values measured from indents beyond the irradiated region (> 5 μm) were averaged (shown as the horizontal line) and the change in hardness, ΔH, was measured with respect to this average value. The scatter in the hardness measured beyond the implanted zone (i.e., > 5 μm) is representative of the uncertainty in the values measured in the implanted zone. Note that the values at the peak (shown as open circles) are not reliable due to the grooving that occurred in the region. The grooving resulted in the

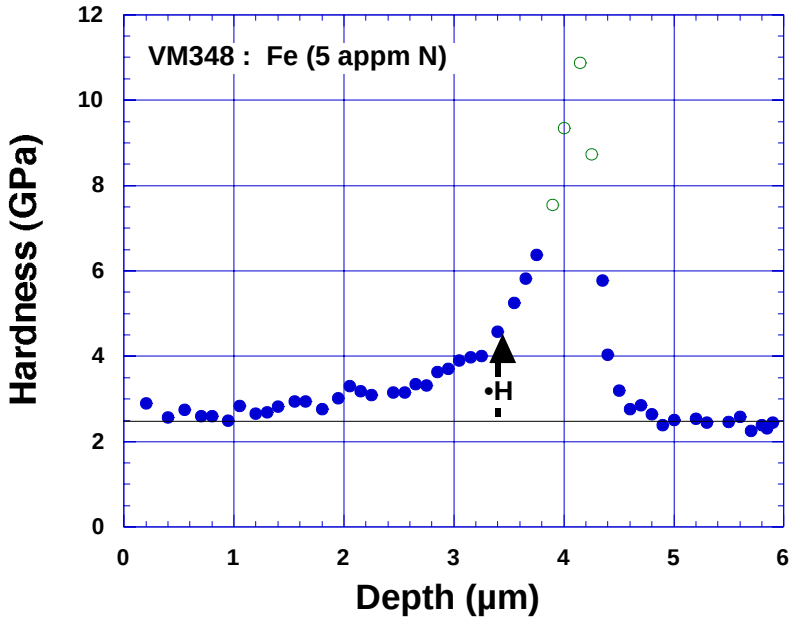

Figure 7. Hardness as a function of distance from the irradiated surface for a typical specimen of alloy VM348 irradiated with 2.5-MeV He ions using indents with ~50 nm contact depths. Values acquired within the grooved portion are marked with open circles to indicate that they have large but unknown errors.

surface not being flat; the area functions of the diamond indenter used to determine the hardness thus have large and unknown errors resulting in unacceptably large uncertainties in the hardness values taken within ± 0.25 μm of the peak.

Measurements similar to those shown in Figure 7 were made for each of the irradiated alloys and are the basis for the hardness-change measurements reported later in the report. Figure 8 provides an example of the measured hardness change on a sample similar to the one shown in Figure 7, along with a corresponding cross-sectional TEM photo to illustrate the general correlation between hardness change and the radiation-induced defect structure. The interface between the irradiated sample and the nickel plating can be seen at a depth of 0. The density of small dislocation loops increases continuously up to the end of the range of the helium beam, at slightly more than 4.1 μm.

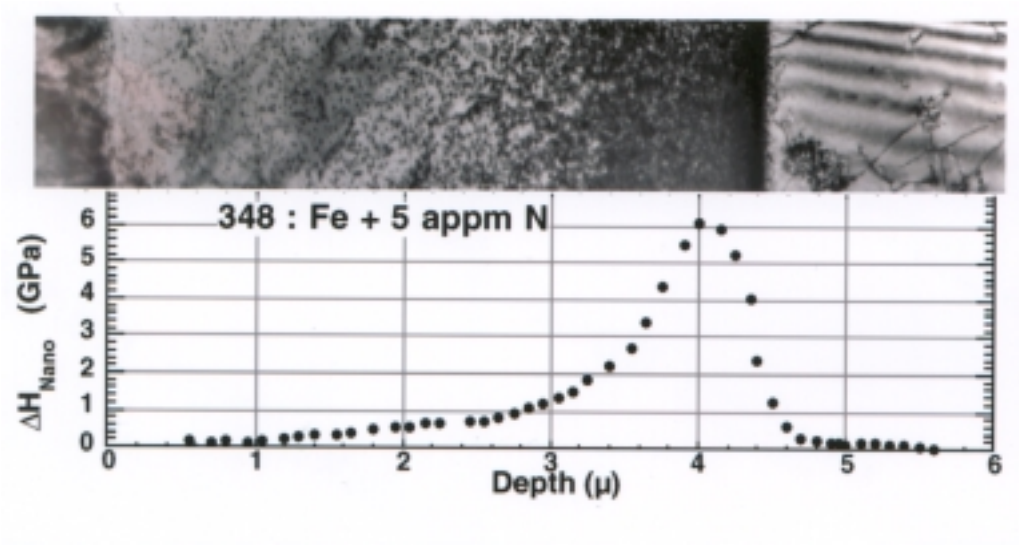

Figure 8. Illustration of the depth dependence of radiation-induced microstructural development and measured hardness change in alloy VM348 (Fe + 5 appm N).

3.3 Electron Microscopy

The TEM examination was carried out using primarily a Philips CM30 microscope operated at 300 kV. Most dislocation-loop imaging was done using **g** = {330} imaging conditions so that the background intensities were weak and the dislocation loops appeared as sharp black spots. The microscope had an energy-dispersive X-ray (EDX) spectrometer capable of detecting elements with Z > 11. All the TEM micrographs appearing in this report were acquired with the CM30 microscope. The specimen thicknesses used to calculate dislocation-loop densities were determined using the X-ray fluorescence method, as described by Kesternich.[8]

Investigation of the chemical content of the precipitates was carried out using a Gatan Imaging Filter (GIF) fitted to the CM30. Energy-filtered imaging was used to determine whether the plate-like precipitates observed in the unirradiated materials were α nitrides or ε carbides, and to verify that the small precipitates observed in the thermally aged materials were rich in copper.[7]

3.4 Summary of Experience from Fe-Ion Irradiations

Three problems inhibited the determination of consistently accurate defect distributions by TEM. The first is the need to have the specimen perforate close enough to the interface to obtain a sufficiently large thin, irradiated area for examination. Secondly, these ferritic steels rapidly form an oxide layer that can inhibit imaging of the smaller radiation-induced defects. Third, the magnetic nature of these materials limits TEM resolution by interfering with the electromagnetic lenses.

In addition, the initial electroplated layer must be chemically and mechanically similar to the substrate material (i.e., Fe) in order to obtain a smooth surface at the interface for nano-indentation and for the electrochemical thinning to consistently give a hole at the interface. To help limit oxide formation at the interface, a “pre-electroplating” cleaning cycle was initially tried. This cleaning was discontinued because it often removed an unknown (but significant) amount of the material, leaving less than 1 μm of irradiated material to work with. This also made greater uncertainties in the dose value assigned to 0.5 μm. The electroplating seemed to build up at a sufficient rate even with the oxide present. In fact, the thin oxide layer actually made it easier to determine the position of the indents below the surface in the SEM.

Indents with 50-nm contact depths were found to give the best results with respect to spatial resolution and minimum scatter. The indents were then finished with 100-nm-deep indentations to make their positions clearly visible in SEM images. The 50-nm depth indents could be separated by as little as 5 μm without interfering with the hardness readings.

Working with only a 1-μm irradiated depth was very constricting both for nano-indentation and TEM imaging. This led to the decision to change the irradiating ions to 2.5-MeV He^+, which penetrate ~4 μm below the specimen surface. This provides a larger volume of material for examination and allows measurement of mechanical and microstructural changes at several doses in each specimen.

4. IRRADIATION CONDITIONS

All the irradiations were carried out using the ORNL Triple Ion Facility[9], with the specimens being irradiated in the form of 3-mm-thick TEM discs at a temperature of ~300^{o}C. The target chamber is capable of irradiating nine TEM discs at a time. Typically, each target included three identical discs of three different alloys. The targets were first heated to approximately 150^{o}C using a electrical resistance heater, and beam heating was used to reach the final irradiation temperature. The temperature of the specimens was measured with a thermocouple spot-welded to the front of one of the target specimens. The TRIM code (versions 91.14 and 92.04)[10] was used to compute the required ion fluences and the displacement dose as a function of depth beneath the specimen surface. The ASTM-recommended average displacement energy of 40 eV[11] was used in the TRIM displacement calculations.

4.1 Iron-ion Irradiations

The specimens were irradiated to peak doses of 0.02, 0.2, and 2.0 dpa, using 4-MeV Fe^{++} ions. Two dpa at the peak corresponds to an ion dose of 1.9×10^{19} ions/m^2. The ion beam current was typically 250 μA/m^2 or ~8×10^{14} ion/m^2/s, corresponding to a peak displacement rate of 8×10^{-5} dpa/s. The longest irradiation time was about 7 h. Figure 9 shows the results of TRIM calculations for these conditions, which indicate that the peak damage occurs at ~1.1 μm below the irradiated surface, and that at 0.5 μm below the surface the dose is about half that at the peak.

4.2 Helium-ion Irradiations

The second set of specimens was irradiated using 2.5-MeV He^{+} ions to a dose of 1.4×10^{21} ion/m^2 at a temperature of ~300^{o}C. The beam current was ~6 mA/m^2 or 3.8×10^{16} ions/m^2/s, and each target was irradiated for a total of ~11 h over 2 days. The depth-dependent displacement rate in these irradiations varied from 2 to 20×10^{-6} dpa/s over the range of depths examined; the dose variations discussed below correspond to measurements made at different depths.

The results from TRIM calculations for the specified He-ion irradiation conditions are shown in Figure 10. The solid line goes with the left axis and shows the damage in dpa as a function of depth in the specimen. Comparison of Figure 10 with Figure 8 illustrates

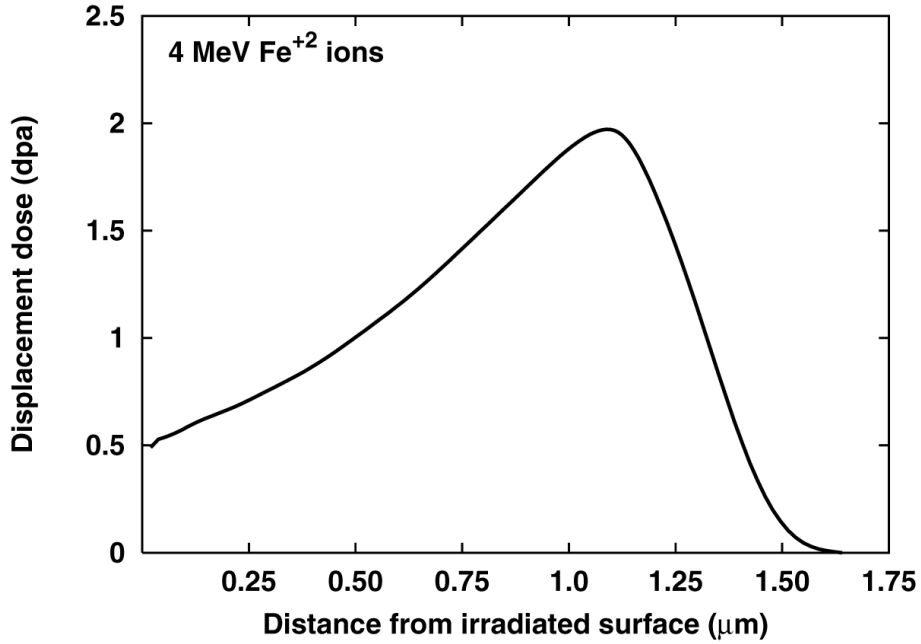

Figure 9. Displacement dose (dpa) as a function of the depth (μm) for 4-MeV Fe ion irradiation of iron as calculated by TRIM.

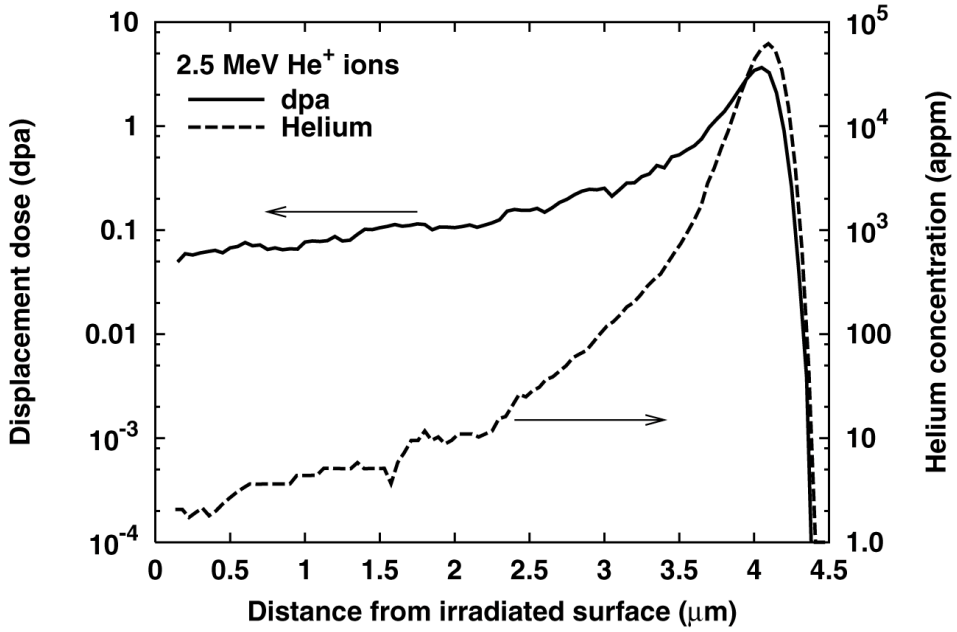

Figure 10. Displacement dose (dpa) and the He concentration from TRIM calculations as function of depth (μm) in an iron specimen irradiated with 2.5-MeV He ions.

the agreement between the calculated and observed damage profiles. At 2-μm depth the dose is ~0.1 dpa; the peak dose of ~3.5 dpa occurs just beyond 4 μm. The dashed line goes with the right axis and shows the implanted He concentration [He] in atomic parts per million (appm) as a function of depth. At the 2-μm position, the helium concentration is 10 appm. The peak helium level of 60,000 appm (6 at-%) occurs near the end of range, just beyond 4 μm. Thus, both dose and helium content are varying. The presence of helium is not completely irrelevant to radiation damage in RPVs because helium is generated in RPV materials by nuclear-transmutation (n,α) reactions, typically at a rate of 0.1 to 1 appm He/dpa. The region around 2-μm depth has a He/dpa ratio of ~100 appm/dpa, which greatly exceeds that obtained under fission neutron irradiation conditions but is of interest for those investigating spallation neutron sources.

5 RESULTS AND DISCUSSION

5.1 Copper Precipitate Formation Under Thermal Aging

Since copper precipitates are believed to be a major cause of hardening in RPV steels, an initial investigation of precipitate hardening was carried out by thermal aging. This was intended to verify that the copper had remained in solution in the high-copper model alloys and to help provide a calibration point for the nano-indentation technique. Discs of the high-Cu alloy VM397 that were 3 mm in diameter and 0.254 mm thick were encapsulated in evacuated ampules and annealed at 550^{o}C for times up to 15 h. The measured hardness change due to copper precipitation is shown as a function of aging time in Figure 11, where each of the nano-indentation data points represents the average of 30 measurements with a 100-nm indent contact depth. For purposes of comparison with the nano-indentation data, 200-g Vickers hardness measurements were also made. The Vickers data are included in Figure 11, along with the results of yield-strength measurements made at UCSB.

The peak hardness change is observed after the 10-h anneal for both indentation techniques and between 5 and 10 h for the tensile measurements. The only significant difference observed between the nano-indentation immurements and the conventional

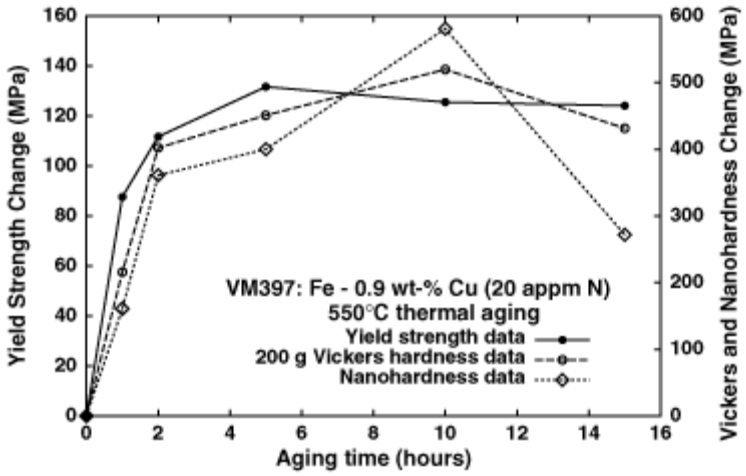

Figure 11. Hardness change as a function of time for alloy VM397 under thermal aging at 550°C.

techniques is for the 15-h aging time, where the material is slightly over-aged. A comparison of these techniques over a broader range of material properties will be discussed below.

The results of these measurements can be compared with the aging study carried out by AEAT on the same alloy.[4] That work employed 20-kg Vickers hardness measurements following aging of thick samples at 500°C. They found a time to peak hardness after about 15 h, with the maximum hardness change being 637 MPa (~65 Vickers hardness units). This compares very favorably with the results shown in Figure 11. The UCSB heat treatment included a short temper at 450°C followed by air-cooling, whereas the AEAT treatment involved quenching directly from the solution treatment. The AEAT heat treatment would retain more of the copper in solution, and this difference could be responsible for the somewhat lower peak Vickers hardness change, ~520 MPa, and the shorter time to peak hardening observed here.

When Cu precipitates form thermally in Fe, they initially have a coherent bcc structure and are not easily visible in TEM. The visibility of the precipitates increases when they change to a heavily faulted fcc or 9R structure after they reach approximately 6 nm in diameter.[12,13] After 5 h of annealing at 550°C, the density of visible Cu precipitates (i.e., the precipitates large enough to change to the 9R structure) was ~1.9×10^{21} m^{-3} and the average diameter was 8.3 nm. The evolution of the precipitate size distribution is illustrated in Figure 12. These size distributions were obtained from TEM micrographs taken down the Z = [111] axis for specimens annealed for 10 and 15 h. The density of visible Cu precipitates (i.e., the precipitates large enough to change to the 9R structure) continued to increase from ~3.2×10^{21} to ~3.6×10^{21} m^{-3}, while the average diameter increased from 8.6 to 10.0 nm between 10 and 15 h.

In order to provide further verification that the precipitates had the expected copper-rich composition, a study was undertaken using the GIF.[7] Energy-filtered images obtained with an Fe-0.9 wt-%Cu specimen are shown in Figure 13. Black arrows point to the same precipitates in both Figure 13(*a*) and 13(*b*). Figure 13(*a*) shows an iron “jump-ratio” image obtained by dividing an image acquired with a 30-eV post-edge window centered at 725 eV by an image acquired with a 30-eV pre-edge window centered at 685 eV. The copper jump ratio image of the same area is shown in 13(*b*), for which the windows were

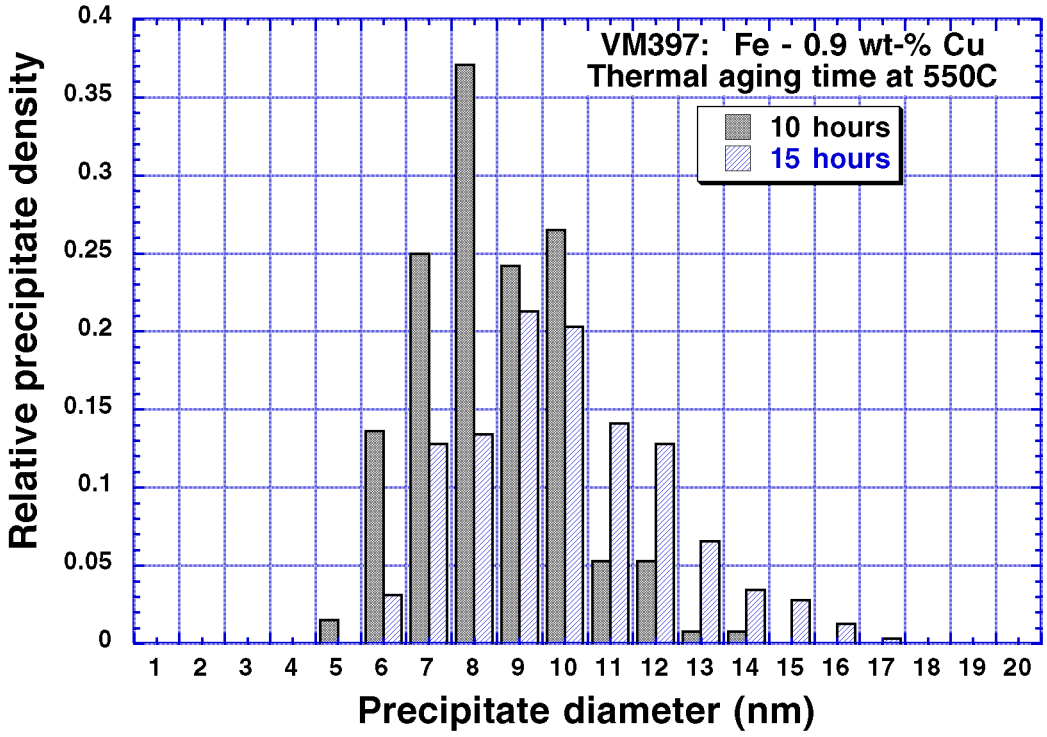

Figure 12. 9R Cu precipitate distribution in alloy VM397 after thermal annealing for 15 h at 550°C.

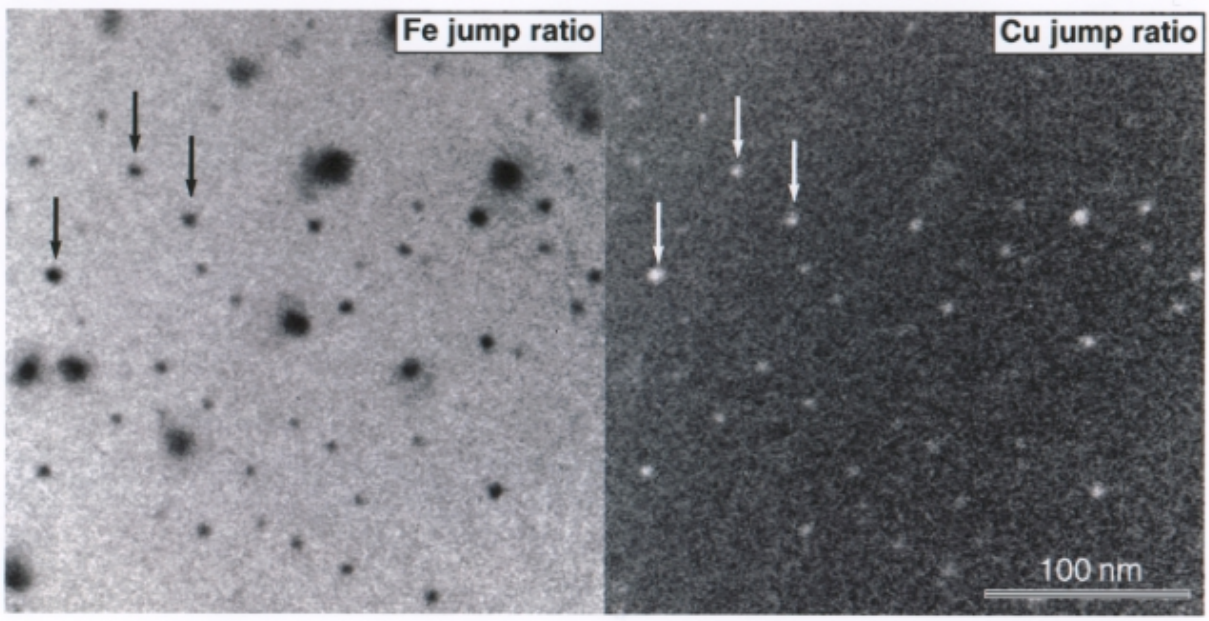

Figure 13. Energy-filtered images of copper precipitates observed in thermally aged Fe-0.9 wt-%Cu. Arrows point out the same precipitates that are shown to be iron-poor in part (*a*) and copper-rich in part (*b*).

centered at 948 and 904 eV. The fact that the precipitates are darkly imaging in 13(*a*) and brightly imaging in 13(*b*) indicates they are deficient in iron and highly enriched in copper.

The Russell-Brown modulus hardening model[14] was used to estimate the hardening arising from the visible Cu precipitates in the annealed specimens. The 15-h results were used as the basis for this evaluation because the highest precipitate density was found in this condition. Good agreement between the model and measured yield strength change could be obtained with reasonable material and microstructural parameters.[15] In order to match the predicted and measured yield strengths, a ratio of the copper precipitate shear modulus to that of the iron matrix was 0.72 and a dislocation density of 2×10^{14} m^{-2} was required. Based on these same parameters, the calculated hardening due to the visible precipitates accounts for only a fraction of the hardening measured for the 5- and 10-h anneal, 0.59 and 0.82, respectively. This indicates that the invisible, coherent bcc portion of the size distribution is responsible for the balance of the hardening change.

5.2 Correlation of Nano-Indentation Hardness Data with Macroscopic Bulk Mechanical-Property Measurements

Experiments were conducted using several ferritic and ferritic/martensitic alloys with varying hardness to correlate the low-load-hardness values determined with a NanoIndenter-II® with the more established macroscopic bulk property measurements.

Specimens for which the yield strengths were already known were chosen so as to span the expected range of the irradiation-induced hardness change. The nine alloys of the VM series (see Section 2) were used (σ_y ~ 150 to 220 MPa) along with the set of thermally aged VM397 specimens mentioned above. These had been annealed at 550°C for 1, 2, 5, 10, and 15 h. Measured yield strengths for tensile specimens that received the same aging treatments were in the range of 250 to 300 MPa. To extend the range over which the hardness change could be correlated, two additional alloys were chosen based on their yield strengths. Alloy A533B, a commercial, fine-grained ferritic alloy with a yield strength of 465 MPa, and HT-9 (12Cr - 1MoVW), a ferritic/martensitic alloy with a yield strength of 750 MPa, were chosen. An example of each of the microstructures is shown in Figure 14, which compares optical micrographs taken at 250× of specimens etched with a 5% HCl solution. The large ferrite grains of VM348,

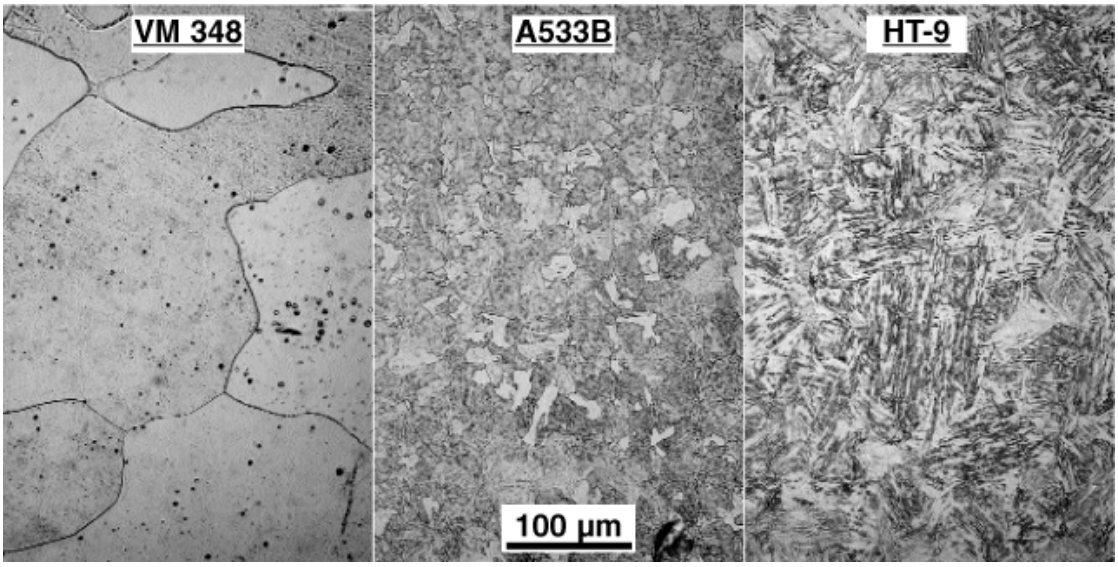

Figure 14. Optical micrographs of etched specimens showing the three typical microstructures of the alloys used in this experiment.

typical of the VM series, are visible in the left image. The small ferrite grains of A533B are visible in the middle image. The martensitic microstructure of the HT-9 alloy is clearly visible in the image on the right. The 100-μm scale marker applies to all three images.

Prior to hardness testing, the specimens were mechanically polished down to 0.05 μm and then electrochemically polished with a perchloric acid solution so that the surface region was flat and damage free. The bulk hardness values were determined by averaging six indents from a commercial Vickers hardness tester using 200-g loads and having indent sizes in the tens of microns. The same specimens were indented to various depths (50, 100, 400 nm) using the nano-indenter with the hardness determined by averaging ten indents at each depth.

The nano-hardness values and the Vickers hardness values are plotted in Figure 15. Nano-hardness values are determined by dividing the maximum load, P_{max}, by the projected contact area, A_{proj}, instead of the actual contact area, A_{con}, which is used in the Vickers definition of hardness. The values for nano-hardness used in the correlation shown in Figure 15 are marked with an asterisk to signify that they were modified by multiplying by the ratio A_{proj}/A_{con} (0.927 for a perfect Berkovich diamond) so that both types of hardness share the same definition. The nano-hardness values show the well-

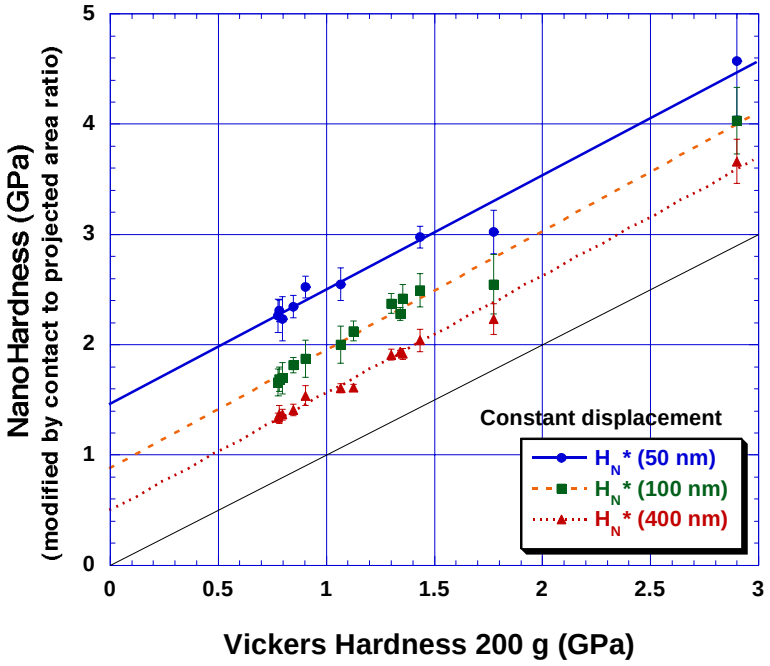

Figure 15. Plot of nano-hardness (measured using constant depth) vs Vickers hardness (measured using a 200-g load) for the same specimens. Note that while the intercepts change, the slopes are very close to 1.0 for all depths.

known apparent increase in hardness with decreasing indent depth.[16] However, the hardness changes are consistent for all the alloys; thus only the intercept, and not the slope of the ΔH_V vs ΔH_N curve changes. The A533B data with a Vickers hardness of ~1.75 GPa show the greatest deviation from the best-fit line shown for the data at each indent depth. Overall, the slope of each line is within a few percent of the bottom solid line, which was drawn with a slope of 1.0.

The maximum load required to indent to a depth of 50 nm differs for each alloy. For the alloys tested here, the range was 0.022 g < P_{max} < 0.043 g. Previously reported comparisons between ultra-low-load hardness and Vickers hardness[17,18] yielded a poorer correlation than that reported here. Because those researchers conducted their nano-hardness measurements using a constant P_{max} instead of constant maximum depth, a further experiment was carried out for purposes of comparison. Using only a subset of five of the alloys, a series of measurements were made with constant P_{max}

instead of depth. Constant maximum loads of 0.05, 0.1 and 1.0 grams were used. This comparison of the modified nano-hardness values and Vickers hardness values is displayed in Figure 16. The one-to-one agreement between Vickers and nano-hardness change is similar to that shown in Figure 15. The lines for the two lowest loads are both within 5 percent of 1.0, while the line with the 1.0-g load has a slope of about 1.1. In this case, the A533B data appear more consistent with the data from the other four alloys.

For these alloys, using <0.05-g loads results in indents with contact depths less than 50 nm and thus the indents have spatial resolution of better than 0.35 μm. Thus, at least for these ferritic and ferritic/martensitic alloys, any change in hardness measured with sub-micron spatial resolution with the nano-indenter is nearly identical to what would have been measured as a bulk property change using a Vickers indenter.

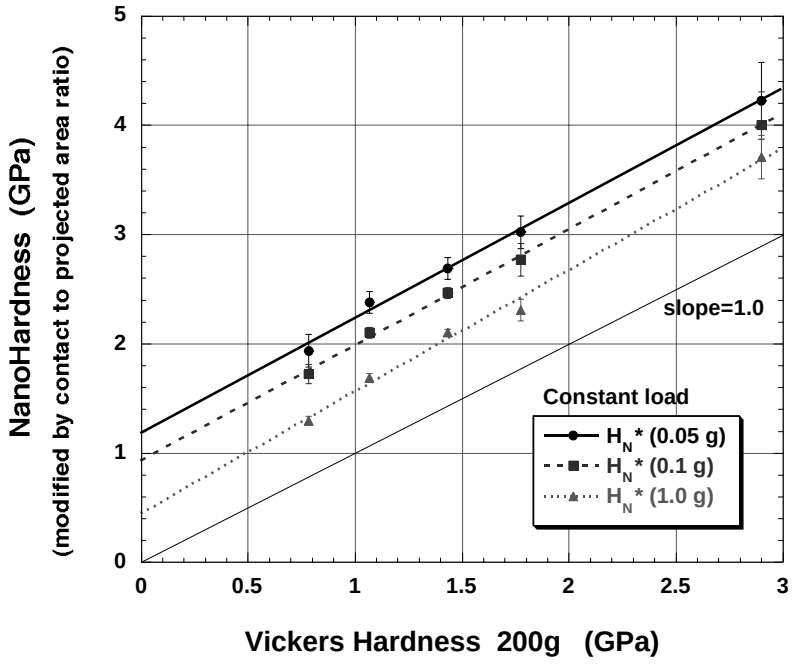

Figure 16. Plot of nano-hardness (measured using constant loads) vs Vickers hardness (measured using a 200-g load) for the same specimens. Note that while the intercepts change, the slopes remain close to 1.0 for all the loads.

The Vickers hardness values for these alloys were also shown to be linearly related to the yield-strength values measured using the usual bulk tensile testing procedures, as shown in Figure 17. The slope of the line relating yield strength to Vickers hardness was found to be 2.79, which compares favorably with other recently published data[19] but is slightly below the traditional value of 3.0.[20]

The successful correlation of the nano-hardness measurements with the bulk mechanical properties is significant not only because of the validation of the nano-indentation technique, but also because of its implications for ion-irradiation studies. This validation permits a broader application of ion irradiations to simulate the environment of nuclear reactors, allowing studies to be carried out without the added complications associated with radioactive specimens. It is possible to use nano-indentation with ultra-low loads to measure changes in hardness with sub-micron spatial resolution across the surface of cross-sectional specimens. Conventional TEM imaging of the cross-sectional specimens allows the defect microstructure to be characterized as a function of depth below the original irradiated surface. For ion irradiations, the dose also varies as a

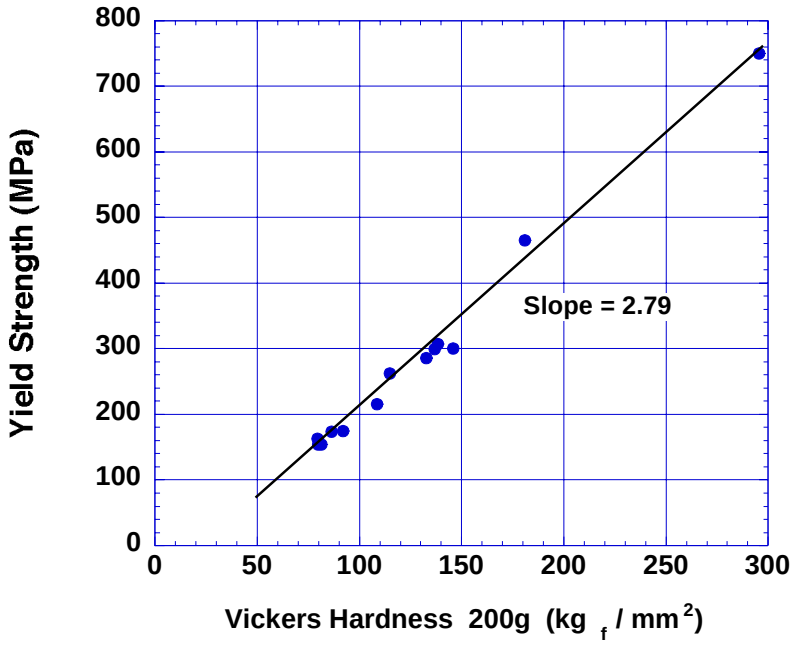

Figure 17. Plot of yield strength vs Vickers hardness (measured using a 200-g load) for the series of alloys.

function of depth in the specimen and can be calculated using standard methods. Thus, changes in hardness and the defect microstructure can be measured and correlated over a range of doses, from a single specimen.

Reliable estimates of mechanical-property changes can be obtained for the high-dose conditions reached at the end of fission reactor lifetimes, without the added complications associated with radioactive specimens. Similarly, the technique can be used to more rapidly screen alloys for irradiation performance and to investigate variables such as alloy composition or thermal-mechanical treatment.

5.3 Iron-Ion Irradiation Results

5.3.1 Hardness Measurements

The effect of copper content on the resultant change in hardness in three low-nitrogen alloys is displayed in Figure 18 for peak doses of 0.02, 0.2, and 2.0 dpa. For the lower doses, all the data fall within a broad scatter band, marked as a shaded region in the

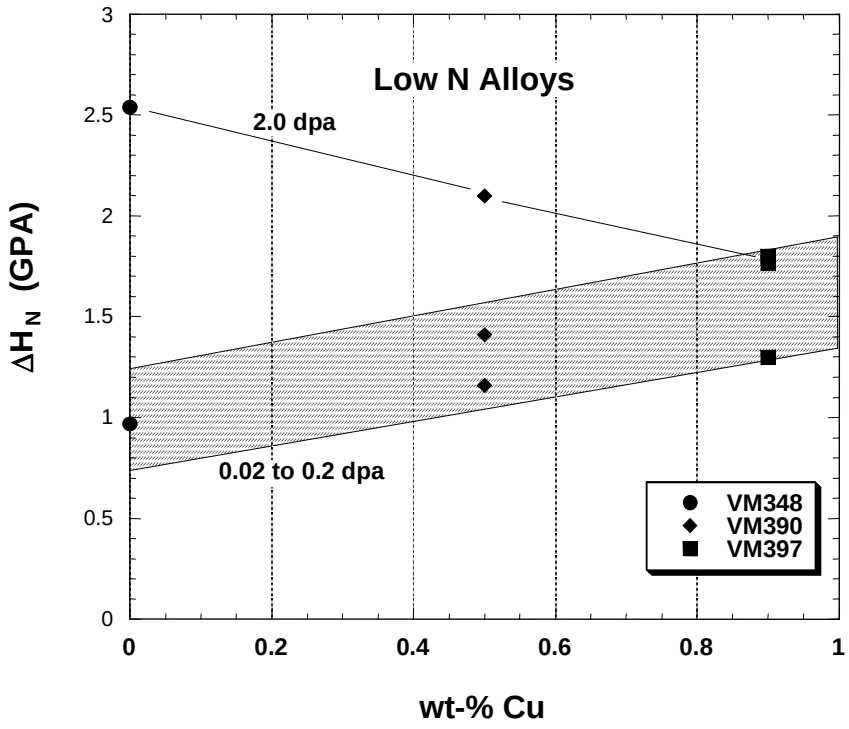

Figure 18. Plot of the change in hardness as function of weight percent Cu for the low-nitrogen alloy.

plot, which is believed to show (within the experimental error of the technique) a linear increase in ΔH with Cu content. The band shows an increase in ΔH of approximately 50% due to the addition of 0.9 wt-% Cu. It is interesting to note that despite the order-of-magnitude increase in dose between the 0.02 and 0.2, there seems to be very little difference in ΔH, suggesting that these low-nitrogen, low-carbon alloys have reached some saturation level of damage at quite low doses.

The hardness values for the highest-dose irradiations, also shown in Figure 18, suggested an inverse dependence of ΔH on copper, inconsistent with the two lower doses. However, the unexpectedly high value of ΔH for the Cu-free alloy occurred only in a very thin region (i.e., it appeared as a very sharp peak on the hardness trace) and may represent phenomena not at work in the lower-dose irradiations. All attempts to make TEM specimens from this sample failed due to poor interface bonding, so it is not known at this time what caused this large increase in hardening. The high-dose irradiation of the alloy with 0.5 wt-% Cu also showed an unusual hardness trace, with increased hardening out to about 3 μm, much deeper than any of the other traces, including that of the high-Cu alloy.

5.3.2 Microstructural Observations

In the high-dose specimens the peak damage region is clearly visible under the proper imaging conditions, even at low magnification. Figure 19 shows a typical defect structure of a high-dose specimen taken with g = ($\bar{3}$30) near the Z = [111] axis. Note the high concentration of “large” defect loops beyond the 1-μm depth, where the implanted ions come to rest.

In the lower-dose specimens, and in the off-peak regions of the high-dose specimens, the defects are only visible at high magnification. It is also often necessary to use weak-beam dark-field imaging (WBDF) to see the defects. High-magnification images (typically ~$10^6\times$) were used in conjunction with a digitizing pad to measure defect distributions. Figure 20 is an example of a measured defect distribution for the Cu-free, high-N alloy VM350. The measurement was made on a WBDF image taken at 2×10^5 magnification and photograghically enlarged to 5 times that value. This specimen was irradiated to

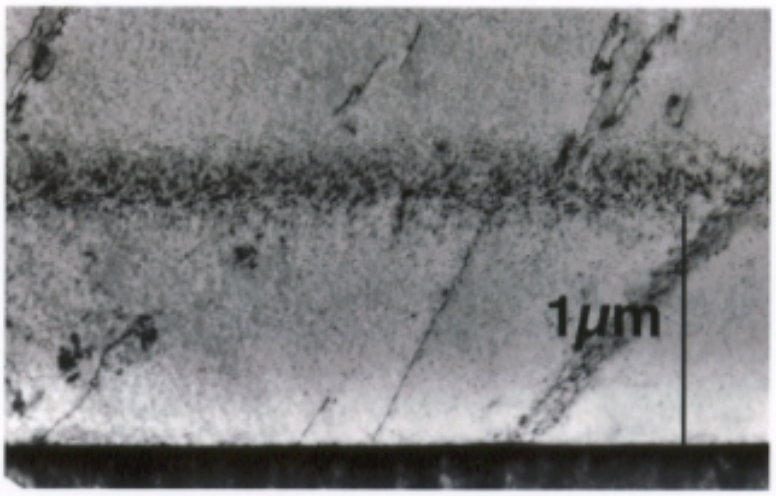

Figure 19. Typical TEM micrograph of a specimen irradiated to 2.0 dpa.

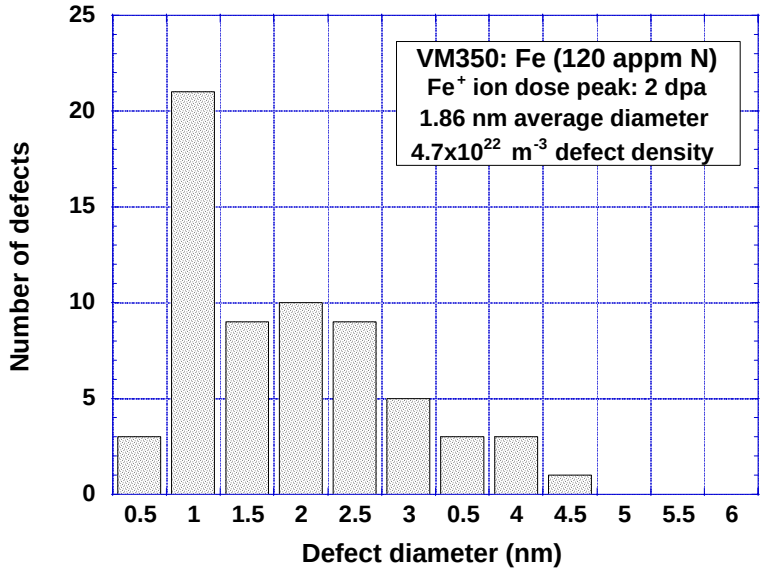

Figure 20. Example of a measured defect distribution for VM350 irradiated to 2.0 dpa.

2.0 dpa at the peak, and the region measured was ~0.7 mm from the interface, just before its peak hardness. The region had a dislocation loop density of 4.7×10^{22} m^{-3}, with an average diameter of 1.86 nm.

5.3.3 Microstructure/Mechanical Property Correlation

In principle, dislocation barrier strengths, α, for defects created by irradiation can be determined by correlating the values for the change in hardness with the defect distributions using a dispersed barrier-hardening model that was first proposed by Orowan.[21] The Orowan hardening equation for calculating the change in shear stress, $\Delta\tau_s$, from a regular array of obstacles is

$$\Delta\tau_s = \alpha G b (Nd)^{0.5}, \quad (1)$$

where G is the shear modulus of the matrix, b is the dislocation Burgers vector (b = a/2 <111>), N is the defect number density, and d is the average defect diameter. The average defect spacing is given by the square-root term in Eq. (1). Various corrections to the Orowan equation have been developed,[22,23] and the currently accepted version is given by Kelly:[23]

$$\Delta\tau_s = \alpha \frac{0.83Gb}{[(Nd)^{-0.5} - d]} \frac{\ln(d/r_o)}{2\pi(1-\nu)^{0.5}}, \quad (2)$$

where ν is Poisson's ratio and r_o is the dislocation core radius. The factor of 0.83 in Eq. (2) accounts for a random distribution of particles, the denominator in the first term corrects the particle spacing for finite particle size, and the final term provides an improved estimate of the dislocation line tension and the interaction between line segments when the dislocation is bowing around an obstacle. Each of these corrections lowers the predicted shear stress, and quite different values of α will be obtained if Eq. (1) is used rather than Eq. (2). Application of Eq. (2) led to a revision of the initial estimates of α published in Ref. 24.

The uniaxial yield strength in polycrystalline materials, $\Delta\sigma_y$, is related to the shear stress by a coefficient known as the Taylor factor,[25] $\Delta\sigma_y = 3.06\Delta\tau_s$, and the work of Cahoon et al.[26] can be used to relate $\Delta\sigma_y$ to the change in Vickers hardness, ΔH_V:

$$\Delta\sigma_y = \left[\frac{1}{3}\Delta H_v (0.1)^n\right] = 3.06\Delta\tau_s, \quad (3)$$

where the work hardening exponent, n, for these alloys was measured using a ball indentation technique[27] and was found to have an average value of n = 0.1. Thus, by using an empirical relation determined by measuring Vickers hardness and nano-hardness for the same as-received alloys (see Section 5.2), it is possible to use Eqs. (2) and (3) to calculate a value for α. The microhardness values need to be multiplied by a factor of 9.81 to convert the units of kg_f/mm^2 to MPa. Using the best-fit line for 100-nm indents from Figure 15 to correlate Vickers and nano-hardness, $\Delta H_v = 1.12\Delta H_N$, the final relationship between nano-hardness and yield strength is

$$\Delta\sigma_y = 0.319\Delta H_N \quad (4)$$

Using the values of ΔH_N = 670 MPa, N = 4.7×10^{22} m^3 and d = 1.8 nm measured for VM350 irradiated to 2 dpa, Eqs. (2–4) yield α = 2.4. The expected value for small dislocation loops is between 0.25 and 0.5,[22] which is much lower than the value obtained from the measured hardness. This indicates that a significant fraction of the hardening arises from defects that remain invisible even at this relatively high dose. A similar result was obtained when the predictions of the Russell-Brown model were compared with the yield-strength measurements for thermally aged VM397 (see Section 5.1). This prevents a confident calculation of barrier strengths and a strict correlation of measured mechanical properties with the observed microstructures. The impact of alloying elements on hardening discussed below will therefore focus on the mechanical property changes and relative changes to the irradiated microstructure.

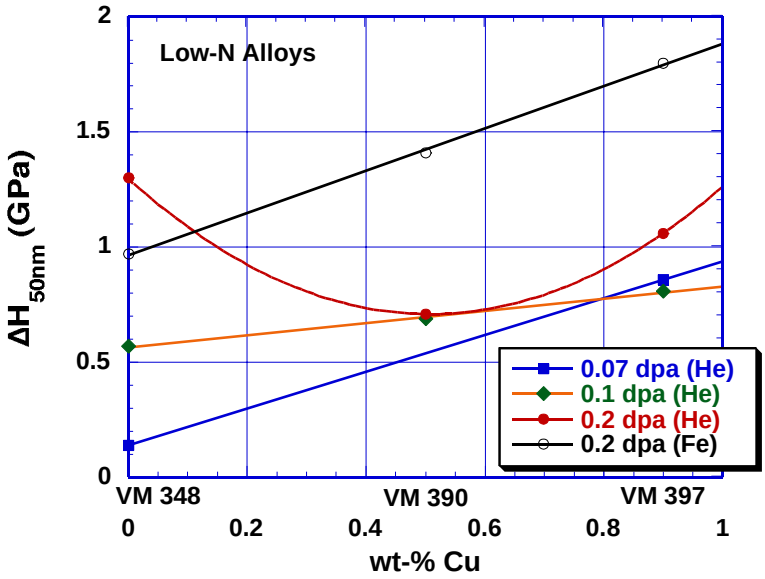

Figure 21. Measured change in hardness as a function of the weight percent copper at three doses for low-nitrogen alloys. The solid points represent data from the He irradiation while the open data points represent data from the Fe irradiation.

5.4 He-Ion Irradiation Results

5.4.1 Hardness Measurements

The selected alloys permitted a range of solute effects to be investigated, and the greater penetration depth of the helium ions improved the spatial resolution of the measurements. Figure 21 is a plot of the change in hardness, ΔH, as a function of wt-% Cu for the low-N alloys at various doses. The solid data points are from the He-irradiated specimens while the open points are the 0.2 dpa data from the earlier Fe irradiation. At a dose of 0.07 dpa the Cu-free alloy shows the least hardening due to the delay (threshold) in the onset of hardening (see below), while at 0.20 dpa it shows the greatest change, due to He bubble formation. At the intermediate dose of 0.1 dpa the dependence of hardness change on copper content appears linear, perhaps fortuitously. The hardness change in the Cu-free alloy shows no tendency to saturate in this dose range while the Cu-containing alloys clearly show a weaker dependence on dose. The change in hardness measured for the Cu-containing alloys irradiated with Fe ions are almost double those observed for He irradiation to similar doses.

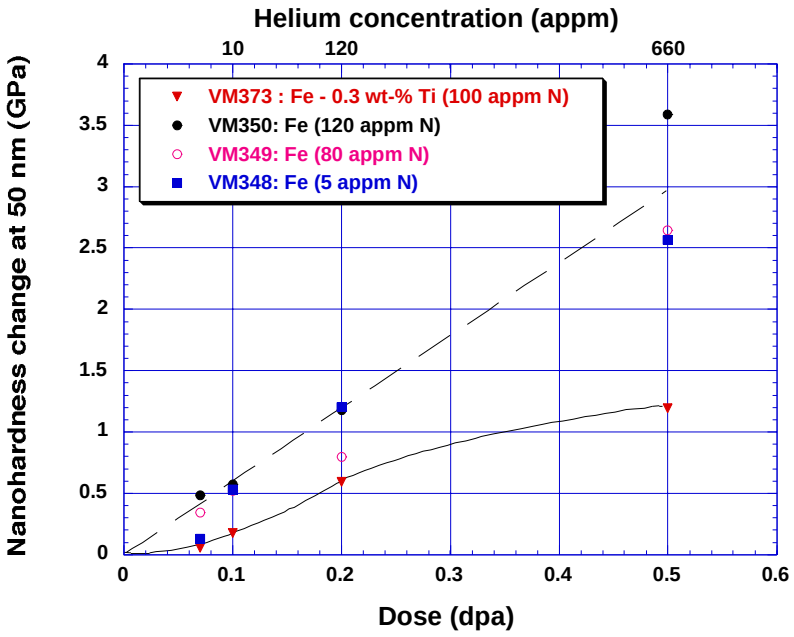

Figure 22. Change in hardness as a function of the dose for the copper-free alloys. The top line represent the average of the Fe-N binary alloys, while the bottom line is for the Ti-containing alloyVM373.

The most significant result of the hardness measurements can be seen by separating the alloys into two categories, Cu-free alloys and Cu-containing alloys. A plot of the change in hardness as a function of dose for the Cu-free alloys is displayed in Figure 22. The indent contact depths were ~50 nm, and each point on the graph represents the average of four or five measurements made within 0.25 μm of the specific depths 1, 2, and 3 μm. The points at the dose of 0.5 dpa were found by averaging only a few points very near a depth of 3.5 μm, which seems reasonable because the change in hardness appeared to be linear in that region. As a result, the uncertainty in the x direction for these high dose points is larger than for the other points in the figures. The values at the end of the range (~4.1 μm) of the He ions are not shown here due to their large, unknown errors.

A single, nearly linear line has been drawn in Figure 22 representing the average change of hardness for the Fe-N binary alloys because of the large scatter, which seemed independent of the nitrogen content at the lower doses. One of the possible reasons for the weakness of the observed effect is the fact that a significant portion of the nitrogen was observed to have precipitated out in all the high-N alloys in the as-received condition

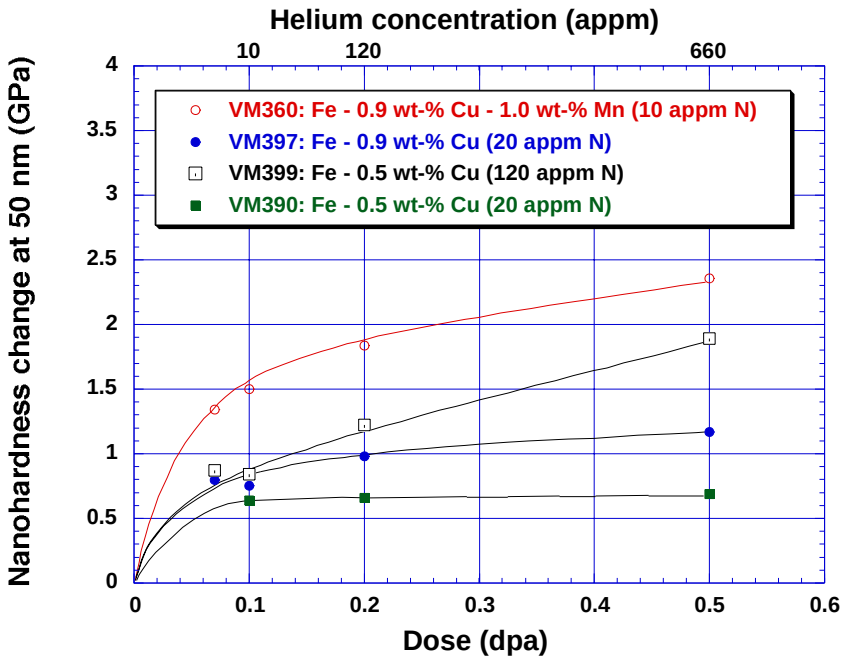

Figure 23. Change in hardness as a function of the dose for the copper-containing alloys. All alloys show a similar supralinear onset of hardening followed by composition-dependent levels of saturation.

with the exception of the titanium-containing alloy, VM373, as reported earlier.[4] However, the effect observed here in the He-irradiated samples was that the addition of nitrogen had little or no effect on the hardening, which is in contrast to the effect observed for the Fe-irradiated samples, in which the addition of nitrogen reduced the change in hardness.

When the data are plotted as a function of the square root of dose, and a linear fit to the points is plotted, the above alloys all show a threshold, or a delay, in the onset of the hardening. This is in marked contrast to the Cu-containing alloys for which the change of hardness is shown in Figure 23. For the Cu-containing alloys there is a rapid hardening at low doses with an apparent saturation at high doses. The addition of either 1 wt-% manganese or 120 appm nitrogen to Fe-Cu binary alloys appears to delay the approach to saturation. When the data for these alloys are plotted as a function of the square root of dose, a linear fit of the data extrapolated back to zero dose shows a common positive ordinate intercept for all the Cu-containing alloys with no indication of a threshold dose.

The point at 0.07 dpa for alloy VM390 is not shown in Figure 23 due to an unfortunate circumstance. Hardness values measured in VM390 for the region with a dose of 0.07 dpa were compromised by a grain boundary running nearly parallel to the irradiated surface.

Comparing alloys VM390 and VM397 shows that an increase in copper increases the change in hardness at all doses. However, of potentially greater interest is the fact that the two low-nitrogen, Cu-containing alloys VM390 and VM397 seemed to be unaffected by the high-He concentrations. The change in hardness for both alloys remained linear, even out to the region with a peak dose of >2 dpa containing 60,000 appm He, and neither alloy showed any tendency to groove at end of range when polished.

The effect of adding a higher nitrogen concentration to the 0.5 wt-% Cu alloy can be seen by comparing alloys VM390 and VM399. The high nitrogen alloy showed a slightly increased ΔH in the low-He region (i.e., $\leq$ 2.5 μm), but a very large ΔH in the high-He region, with the groove forming at the end of range during the polishing procedure. The fact that the high nitrogen level in VM399 seems to slow the approach to saturation observed in VM390 is consistent with the greater effect of nitrogen at the highest dose shown in Figure 22 for VM350.

Comparing alloys VM360 with VM397 shows that the addition of 1 wt-% Mn to the Fe matrix, in conjunction with the 0.9 wt-% Cu, nearly doubles the change in hardness due to the irradiation at all doses. The hardening appears to saturate at a much higher level, and the approach to saturation is slower in the manganese-containing material. The VM360 alloy was also observed to groove at the end of range during the polishing process.

5.4.2 Microstructural Observations

5.4.2.1 Dislocation loop formation

The defect microstructure in each of the irradiated alloys was investigated in cross section using conventional TEM imaging techniques. Figure 24 shows a survey of the cross-sectional, low-magnification micrographs of the irradiated region for most of the alloys. The alloy numbers and their compositions are listed at the base of each micrograph, and the depth scale is shown on the right-hand side of the figure. Alloy

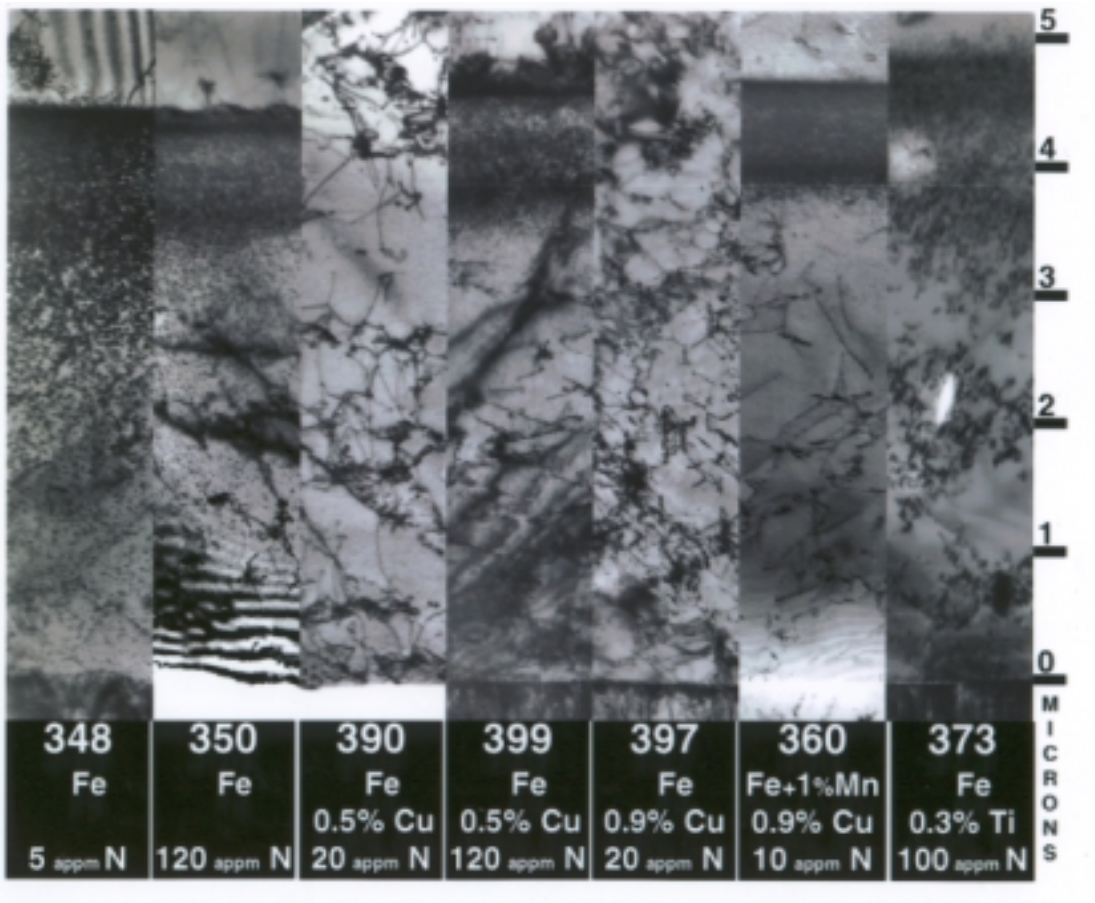

Figure 24. A survey of the low-magnification cross-sectional TEM micrographs showing the entire irradiated region of the major alloys. The scale is on the left and the alloy contents are listed below each image. Note that alloys VM390 and VM397 show no obvious irradiation damage even at the end of range of the He ions.

VM349 is not included because it is so similar to alloy VM350. All the alloys that showed grooving when polished for nano-indentation show an extremely high defect density at the end of range of the He ions, at and beyond 4 μm. The two low-N, Cu-containing alloys, VM390 and VM397, show no such peak damage region.

Higher-magnification micrographs of the defect structures at the 2-μm-depth region (i.e., 0.1 dpa and [He] = 10 appm) are shown in Figures 25 and 26. The scale markers found in the upper left quadrants apply to all the images in the figures. The images do not represent the same thickness, and thus the reader is cautioned against drawing any conclusions about the density of the defects shown in the figures, but to compare defect

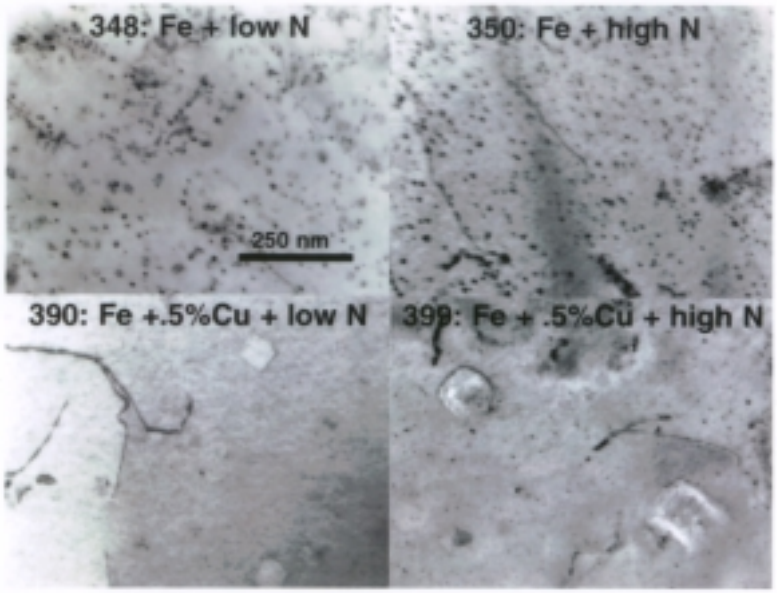

Figure 25. TEM micrographs of several of the alloys taken at approximately 2-μm depth (0.1 dpa). Comparing left to right shows the effect of nitrogen on the defect distribution. Comparing top to bottom shows the effect of 0.5 wt-% copper on the defect distribution.

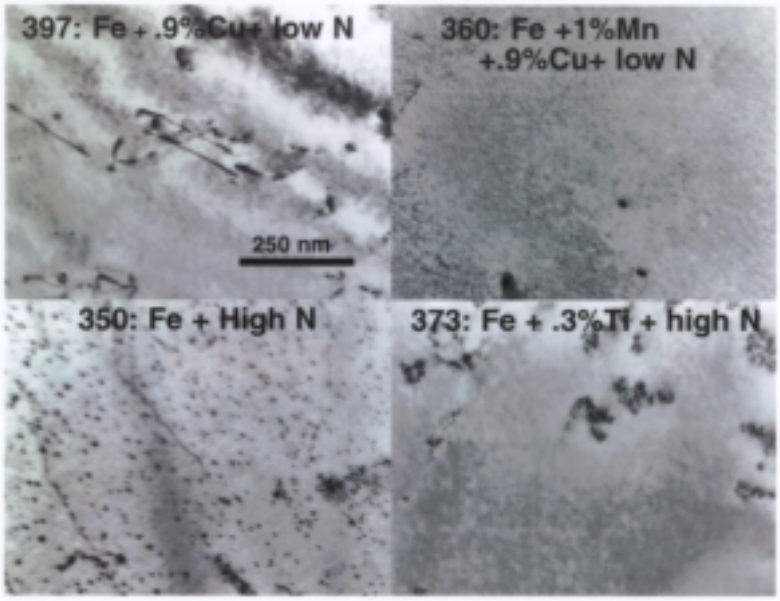

Figure 26. TEM micrographs of several of the alloys taken at approximately 2-μm depth (0.1 dpa). Comparing left to right shows the effect of Mn (top row) and Ti (bottom row) on the defect distribution.

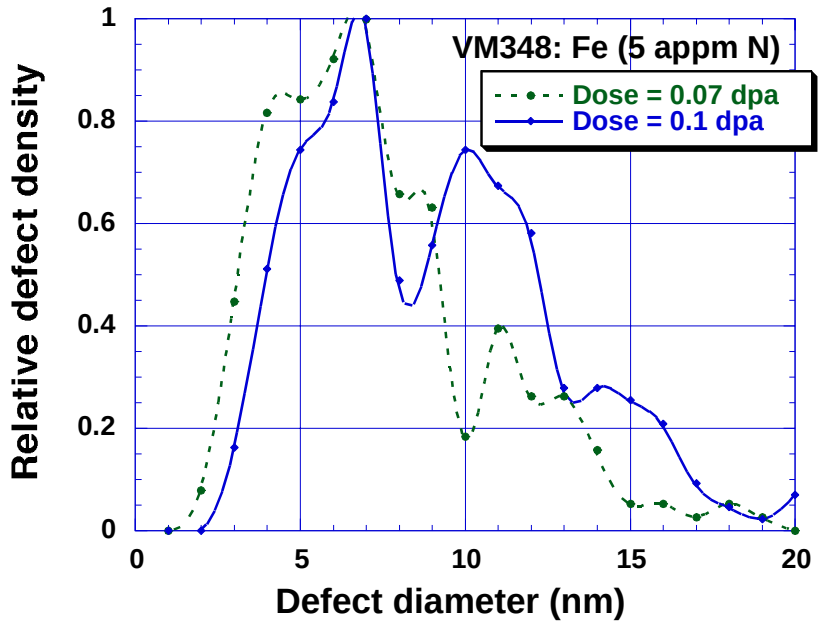

Figure 27. Measured defect distributions for alloy VM348 at two different doses.

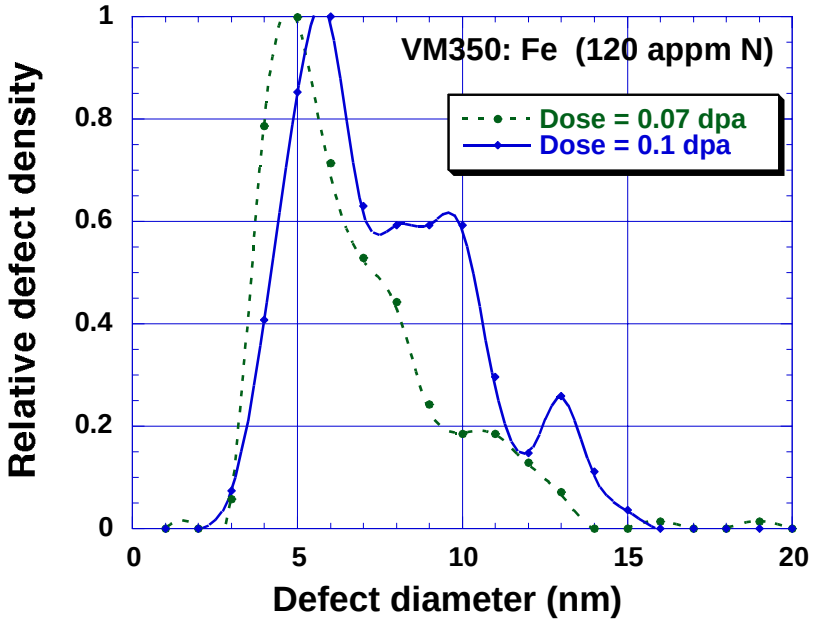

Figure 28. Measured defect distributions for alloy VM350 at two different doses.

sizes only. Comparing alloys VM348 and VM350 shows that the increase in nitrogen content seems to have slightly decreased the average size of the dislocation loops. Figures 27 and 28 are plots of the measured defect distributions for two depths (i.e., doses) for the alloys VM348 and VM350, respectively. The increase in nitrogen in alloy VM350 indeed resulted in slightly smaller dislocation loops. A comparison of the distributions for each alloy indicates that loop growth occurs with increasing dose.

The damage structure was much coarser in the helium-ion-irradiated specimens than in those irradiated with iron ions. For example, the average loop diameter in VM350 was 7.7 nm, and the density was 2.95×10^{22} m^{-3} at a helium dose of 0.1 dpa, whereas d = 1.86 nm and N = 4.7×10^{22} m^{-3} for iron irradiation to 2 dpa. This difference may arise from differences in defect nucleation rates because the point-defect supersaturation would be much higher in the case of the iron irradiation. An effective dislocation barrier strength of ~0.5 was obtained from the hardness and microstructural values measured in VM348 and VM350 at 0.07 and 0.1 dpa. This is closer to the expected value mentioned above, but still indicates the presence of hardening from defects too small to be resolved in TEM.

Comparisons if alloys VM390 and VM397 with VM348 show that the addition of 0.5 or 0.9 wt-% Cu (while maintaining low N) seems to have suppressed the formation of any visible defects (i.e., dislocation loops or point-defect clusters present must have a diameter less than 2 nm). Because hardening tends to increase with copper content as shown in Figure 21, it is clear that the hardening measured in alloys VM390 and VM397 is caused by defects that are too small to be seen by TEM. As a result, the ability to perform the desired correlation of mechanical-property changes with TEM microstructural measurements is even more severely compromised in the copper-containing materials.

A comparison of alloy VM399 with VM390 shows that when sufficient nitrogen is added to the FeCu alloy, irradiation causes dislocation loops to form that are large enough to be visible (d > 2 nm). Similarly, comparison of alloy VM360 with VM397 shows that the addition of Mn to the matrix also results in visible dislocation loops. Although they are just barely visible (d ~ 2 nm) there is definitely a higher loop density present in VM397 than in

any of the other alloys. This high density of very small dislocation loops correlates well with alloy VM360, showing the greatest change in hardness in the low-dose, relatively low-He region ($\leq$ 2.5 μm).

A comparison of alloy VM373 with VM350 shows that the addition of 0.3 wt-% Ti to the matrix resulted in a suppression of dislocation loop formation but apparently led to precipitation in the irradiated zone. This result is interesting because alloy VM373 was the only high-N alloy to retain nitrogen in solution in the as-received state, and it showed the least hardening of all the alloys in the low-dose, relatively low-He region ($\leq$ 2.5 μm). Further work would be required to verify that the defects are a second phase and to identify their type.

5.4.2.2 Observations of helium bubble formation

All the alloys with the exception of the low-N, Cu-containing VM390 and VM397, show extensive He bubble formation in the region beyond 3.75 μm (i.e., [He] $\geq$ 3000 appm). All the bubbles showed a tight size distribution centered at d~2 nm. Even at the highest He concentration of ~60,000 appm, the bubble density increased but the size of the bubbles remained similar. A close investigation of the He bubbles as a function of depth in the VM348 (Fe + low-N) alloy revealed that while there were a few bubbles formed at 2 μm ([He] = 10 appm), significant formation did not occur until beyond 3 μm ([He] = 120 appm). Figure 29 shows the He bubbles in the VM348 alloy at a depth of 3.5 μm (dose = 0.5 dpa, and [He] = 660 appm) using Fresnel fringe contrast. In the underfocused condition the bubbles appear as bright in the center with a dark outer fringe, while in the overfocused condition they appear dark with a bright outer fringe.

It is of significant interest that alloys VM390 and VM397 showed no bubble formation, even at the end of range where [He] = 60,000 appm. Because these two alloys were irradiated in separate targets and with other alloys (390 with VM348 and VM399, and VM397 with VM350 and VM387), it is clear that the apparent absence of bubbles is due to the effect of chemical composition, not to differences in irradiation conditions. Both alloys showed an increase in hardness as a function of depth and no tendency to groove. To demonstrate that the helium was present a post-irradiation anneal was performed on a VM397 specimen at 600^{o}C for 24 h. It resulted in extensive bubble/void formation at the end of range depth. Evidently, copper diminishes the availability of vacancies during

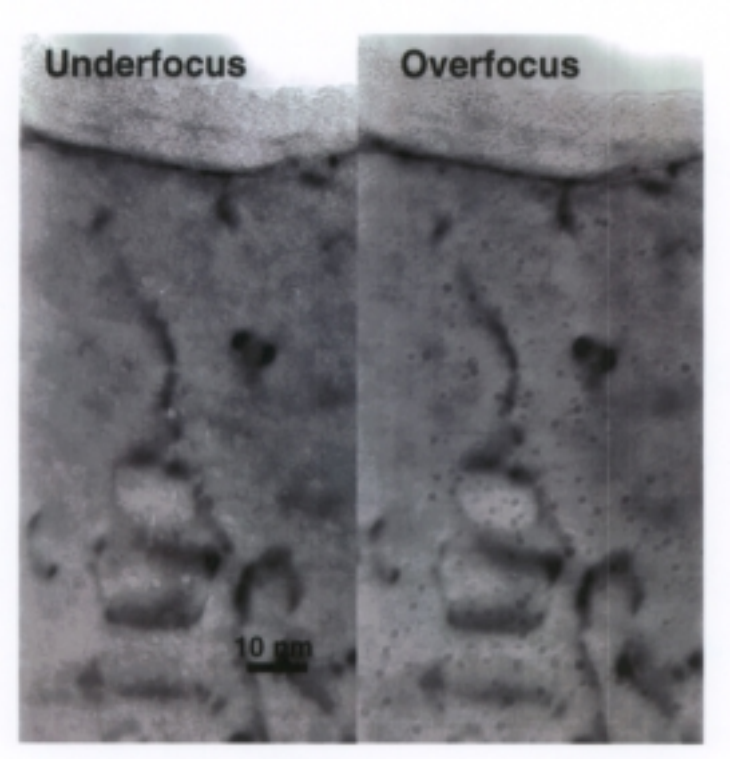

Figure 29. TEM micrographs of the He bubble formation in alloy VM348 irradiated to a dose of 0.5 dpa and a He concentration of 660 appm.

irradiation. This surprisingly strong Cu-vacancy interaction is consistent with a postulated high-copper-vacancy binding energy but may be much greater in a clean Fe-Cu binary alloy.[28-30] This ability of the copper to suppress He bubble formation appears to be negated by either the addition of a substitutional solute like Mn (see alloy VM360), or an interstitial solute like N (see alloy VM399). This is similar to the effect of nitrogen observed in positron lifetime measurements, which were made following isochronal annealing experiments with these alloys.[5] Addition of nitrogen to the Fe-Cu binary alloy significantly reduced the measured positron lifetime.

6 SUMMARY

The primary results of this study have demonstrated the capabilities and limitations of the techniques employed. The relatively high doses reached here in several materials would have been difficult to obtain in a timely way from neutron irradiations, and it would not have been possible to perform the extensive TEM examination of the irradiated microstructure if the materials had been radioactive.

The primary conclusions of this work are summarized as follows.

1. Hardness changes measured with loads as low as 0.05 g were shown to be well correlated with conventional Vickers microhardness measurements with a 200-g load. This indicates that the low-load hardness measurements warrant further investigation of their potential use.
2. The dose and compositional dependence of the hardening change measured with the nano-indentation technique on ion-irradiated specimens was consistent with that obtained from more conventional mechanical property measurements following neutron irradiation.
3. A consistent difference between the copper-containing and the copper-free alloys was observed. The hardness change measured in copper-containing alloys exhibited a greater tendency to saturate at high doses.
4. The saturation hardness level in the copper-containing alloys increased with copper content, increased with the addition of nitrogen, and increased with the addition of manganese.
5. Although the helium ion irradiation led to the excessive amounts of implanted helium, it also provided evidence of a very strong interaction between copper and radiation-induced vacancies. Bubble formation was observed in most specimens as the helium stabilized and promoted the growth of vacancy clusters. However, bubble formation was not observed in the two low-nitrogen Fe-Cu binary alloys, presumably because strong Cu-vacancy binding prevented bubble growth. The addition of either interstitial or substitutional solutes mitigates the Cu-vacancy binding interaction, leading to visible bubble formation.

6. The TEM microstructural characterization indicates that addition of copper leads to a refinement of the radiation-induced microstructure. This is consistent with the copper-vacancy interaction just mentioned, and similar observations have been made by other researchers.[31] Conversely, addition of interstitial nitrogen or substitutional manganese leads to an increase in the size of the visible defects in the copper-containing alloys.
7. Although many of the difficulties inherent in high-magnification TEM examination of magnetic materials were overcome in this work, it was not possible to make a one-to-one correlation between microstructural changes and hardness changes due to the hardening induced by defects that remain below the resolution limit of the microscope. In particular, significant hardening was measured in the low-nitrogen, Fe-Cu binary alloys while no defects were visible by TEM.

7 REFERENCES

1. W.C. Oliver, and G.M. Pharr, Journal of Materials Research, 7 (6), 1564 (1992).

2. L. K. Mansur, Nuclear Technology, 40, 5, 1978.

3. G.R. Odette, G. E. Lucas, R. D. Klingensmith, and R. E. Stoller, “On the Effect of Flux and Composition on Irradiation Hardening at 60°C,” pp. 547-568 in *Effects of Radiation on Materials: 17th International Symposium*, ASTM STP 1270, D. S. Gelles, R. K. Nanstad, A. S. Kumar, and E. A. Little, Eds., American Society for Testing and Materials, Philadelphia, 1996.

4. J. Mace and W.J. Phythian, AEA Technology, Harwell, U.K., *AEA/UCSB Model FeCuMn Alloys Results Compendium: Grain Size and 550°C Age Hardening Response*, AEA Technology Report, AEA-RS-2148, December 1991.

5. W.J. Phythian, N. de Diego, J. Mace and R. J. McElroy, “Characterization of Model Fe-Cu-Mn-Ti-N Alloys by Electron Microscopy and Positron Annihilation,” pp. 462-491 in *Effects of Radiation on Materials: 16th International Symposium*, ASTM STP 1175, A. S. Kumar, D. S. Gelles, R. K. Nanstad, and E. A. Little, Eds., American Society for Testing and Materials, Philadelphia, 1993.

6. P. M. Rice and R. E. Stoller, Oak Ridge National Laboratory, Oak Ridge, Tenn., *Microstructural Characterization of Selected AEA/UCSB Model FeCuMn Alloys*, USNRC Report NUREG/CR-6332 (ORNL/TM-12980), June 1996.

7. P. M. Rice, R. E. Stoller, and J. Bentley, “Energy-Filtered Imaging of Precipitates in FeCuN Alloys,” *Microscopy and Microanalysis 1995*, G. W. Bailey, M. H. Ellisman, R. A. Hennigar, and N. J. Zaluzec, Eds., Microscopy Society of America, Jones and Begell Publishing, New York, 1995, pp. 542-543.

8. W. Kesternich, Electron Microscopy, Vol. 2, (1984), pp. 837-38.

9. M.B. Lewis, W. R. Allen, R.A. Buhl, N.H. Packan, S.W. Cook, and L.K. Mansur, “Triple Ion Beam Irradiation Facility,” Nuclear Instruments and Methods in Physics Research B43, (1989) 243-253.

10. J.P. Biersack and L.G. Haggmark, Nuclear Instruments and Methods, 174, 257 (1980).

11. ASTM E521-89, Neutron Radiation Damage Simulation by Charged-Particle Irradiation, ASTM Book of Standards 12.02, (1990).

12. P.J. Othen, M.L. Jenkins, G.D. Smith, and W.J. Phythian, Philosophical Magazine Letters 64 (1991) 383-391.

13. W.J. Phythian, A. J. E. Foreman, C. A. English, J. T. Buswell, M. Hetherington, K. Roberts, and S. Pizzini, “The Structure and Hardening Mechanism of Copper Precipitation in Thermally Aged or Irradiated Fe-Cu and Fe-Cu-Ni Model Alloys,” pp. 131-150 in *Effects of Radiation on Materials: 15th International Symposium*, ASTM STP 1125, R. E. Stoller, A. S. Kumar, and D. S. Gelles, Eds., American Society for Testing and Materials, Philadelphia, 1992.

14. K. C. Russell and L. M. Brown, Acta Metallurgica 20 (1972) 969-974.

15. R. E. Stoller, Oak Ridge National Laboratory, Oak Ridge, Tenn., *A Comparison of the Relative Importance of Copper Precipitates and Point Defect Clusters in Reactor Pressure Vessel Embrittlemen*t, NUREG-CR/6231, (ORNL-6811), December 1993.

16. J. B. Pethica, R. Hutchings, and W. C. Oliver, “Hardness Measurements at Penetration Depths as Small as 20 nm,” Philosophical Magazine A 48 (1983) 593-606.

17. K. Yasuda, K. Shinohara, C. Kinoshita, M. Yamada, and M. Arai, “Development of the ultra-microhardness techniques for evaluating stress-strain properties of metals,” Journal of Nuclear Materials, 212-215, pp1698-1702, 1994.

18. K. Shinohara, K. Yasuda, M. Yamada, and C. Kinoshita, “Universal Method For Evaluating Work-Hardening Exponent of Metals Using Ultra-Microhardness Tests,” Acta Metallurgica et Materiala, Vol. 42, (11), pp. 3909-3915, 1994.

19. K. Osamura, H. Okuda, S. Ochiai, M. Takasjima, K. Asano, M. Furusaka, K. Kishida, and F. Kurosawa, “Precipitation Hardening in Fe-Cu Binary and Quaternary Alloys,” ISIJ International, vol. 34 (4), pp. 359-365, 1994.

20. D. Tabor, “The Hardness of Metals,” Oxford University Press, London, 1951.

21. E. Orowan, in "Internal Stresses in Metals and Alloys," The Institute of Metals, London, 1948, pp. 451-453.

22. A. L. Bement, Jr., in Strength of Metals and Alloys, Proc. of 2nd Int. Conf., ASM International, Metals Park, OH, 1973, pp. 693-7288.

23. P. M. Kelly, International Metallurgical Reviews 18, 31 (1973)

24. P. M. Rice, R. E. Stoller, B. N. Lucas, and W. C. Oliver, “Microstructural and Mechanical Property Changes in Model Fe-Cu Alloys,” *Microstructure of Irradiated Materials*, Vol. 373, I. M. Robertson, L. E. Rehn, S. J. Zinkle, and W. J. Phythian, Eds., Materials Research Society, Jones

25. U.F. Kocks, Metallurgical Transactions 1, 1121 (1970).

26. J.R. Cahoon, W.H. Broughton, and A.R. Kutzak, Metallurgical Transactions 2, 1979 (1971).

27. F.M. Haggag, R.K. Nanstad, and D.N. Braski, in *Innovative Approaches to Irradiation Damage, and Fracture Analysis*, D.L. Marriott, T.R. Mager, and W.H. Bamford, Eds., (ASME Book No. H00485, 1989) PVP 170, pp.101-107.

28. G. Salje, and M. Feller-Kniepmeier, Journal of Applied Physics 48 (5) (1977) 1833.

29. G. R. Odette, and C. K. Sheeks, in: *Phase Stability During Irradiation*, J.R Holland, L.K. Mansur, and D.I. Potter, Eds., (The Metallurgical Society of AIME, Warrendale, PA, 1981) p. 416.

30. A. Moslang, E. Albert, E. Recknagel, A. Weildinger, and P. Moser, Hyperfine Interactions, 15/16 (1983) p. 409.

31. F. Ebrahimi, D. T. Hoelzer, D. Venables, and V. Krishnamoorthy, Materials Engineering Associates Inc., Lanham, MD, *Development of a Mechanistic Understanding of Radiation Embrittlement in Reactor Pressure Vessel Steels*, USNRC Report NUREG/CR-5063, (MEA-2268), 1988.

INTERNAL DISTRIBUTION

1. B. R. Bass
2. E. E. Bloom
3. S. K. Iskander
4. L. K. Mansur
5. M. K. Miller
6. R. K. Nanstad
7. C. E. Pugh

8-12. T. M. Rosseel
13. A. F. Rowcliffe
14. M. A. Sokolov
15. S. Spooner
16-25. R. E. Stoller
26. Laboratory Records (RC)
27-28. Laboratory Records (OSTI)

EXTERNAL DISTRIBUTION

29-30. AEA TECHNOLOGY-HARWELL, Thermal Reactor Services, Didcot, Oxfordshire OX11 OR, United Kingdom

C. A. English
J. Hyde

31. ATI, Inc., Suite 160, 210 Crow Canyon Place, San Ramon, CA 94583

W. L. Server

32. CEGB (Nuclear Electric), Berkeley Nuclear Labs., Berkeley, Gloucestershire GL 139 PB, United Kingdom

C. J. Bolton

33. CEN/SCK, Belgium, Reactor Physics Department, Boeretang 200, B-2400MOL, Belgium

E. VanWalle

INTERNAL DISTRIBUTION

1. B. R. Bass
2. E. E. Bloom
3. S. K. Iskander
4. L. K. Mansur
5. M. K. Miller
6. R. K. Nanstad
7. C. E. Pugh

8-12. T. M. Rosseel
13. A. F. Rowcliffe
14. M. A. Sokolov
15. S. Spooner
16-25. R. E. Stoller
26. Laboratory Records (RC)
27-28. Laboratory Records (OSTI)

EXTERNAL DISTRIBUTION

29-30. AEA TECHNOLOGY-HARWELL, Thermal Reactor Services, Didcot, Oxfordshire OX11 OR, United Kingdom

C. A. English
J. Hyde

31. ATI, Inc., Suite 160, 210 Crow Canyon Place, San Ramon, CA 94583

W. L. Server

32. CEGB (Nuclear Electric), Berkeley Nuclear Labs., Berkeley, Gloucestershire GL 139 PB, United Kingdom

C. J. Bolton

33. CEN/SCK, Belgium, Reactor Physics Department, Boeretang 200, B-2400MOL, Belgium

E. VanWalle

34. ELECTRICITE DE FRANCE, DEPARTMENT EMA, Les Renardieres, Route de Sens, B.P. I. Ecuelles, 77250 moret sur loing, France

J. C. Van Duysen

35-39. IBM Research Division, Almaden Research Center, 650 Harry Road, K19A/D1, San Jose, CA 95120-6099

P. M. Rice

40-41. JAPAN ATOMIC ENERGY RESEARCH INSTITUE, Reactor Component Reliability Laboratory, Department of Nuclear Safety Research, Tokai-mura, Ibaraki-ken, 319-11, Japan

M. Suzuki
K. Oniza

42-46. NRC, RES/Division of Engineering Technology, Washington, DC 20555

C. J. Fairbanks
E. M. Hackett
M. T. Kirk
S. N. Malik
M. E. Mayfield

47. ROLLS-ROYCE AND ASSOCIATES LTD., P.O. Box 31, Raynesway, Derby, England

T. J. Williams

48. TECHNICAL RESEARCH CENTRE OF FINLAND (VTT), Metals Laboratory, P.O. Box 26, SF-02151 Espoo (Kemistinite 3, 02150 Espoo), Finland

M. Valo

49. UNIVERSITE DE ROUEN, 76128 Mont St. Aignan, CEDEX, France

P. Pareige

50-51. UNIVERSITY OF CALIFORNIA, Department of Chemical and Nuclear Engineering, Ward Memorial Drive, Santa Barbara, CA 93106

G. E. Lucas
G. R. Odette

52-53. UNIVERSITY OF MICHIGAN, Nuclear Enginnering and radiological Sciences, 1906 Cooley Building, Ann Arbor, Michigan 48109-2104

G. S. Was
Lu-Min Wang

54. UNIVERSITY OF OXFORD, Department of Materials, Parks Road, Oxford OX13PH, United Kingdom

M. L. Jenkins

55-56. WESTINGHOUSE SCIENCE AND TECHNOLOGY CENTER, 1310 Beulah Road, Pittsburgh, PA 15235

M. G. Burke
R. G. Lott

57. DOE, DIVISION OF MATERIALS SCIENCES, ER-131, MS GS-236/GTN, Washington, DC 20585

R. J. Gottschall

58. DOE OAK RIDGE OPERATIONS OFFICE, P.O. Box 2008, Oak Ridge, TN 37831-6269

Sherman Martin

59-120. Given distribution as shown in category R5 (NTIS-10)